SSCL-Preprint-147

SSCL-Preprint-147

Superconducting Super Collider Laboratory

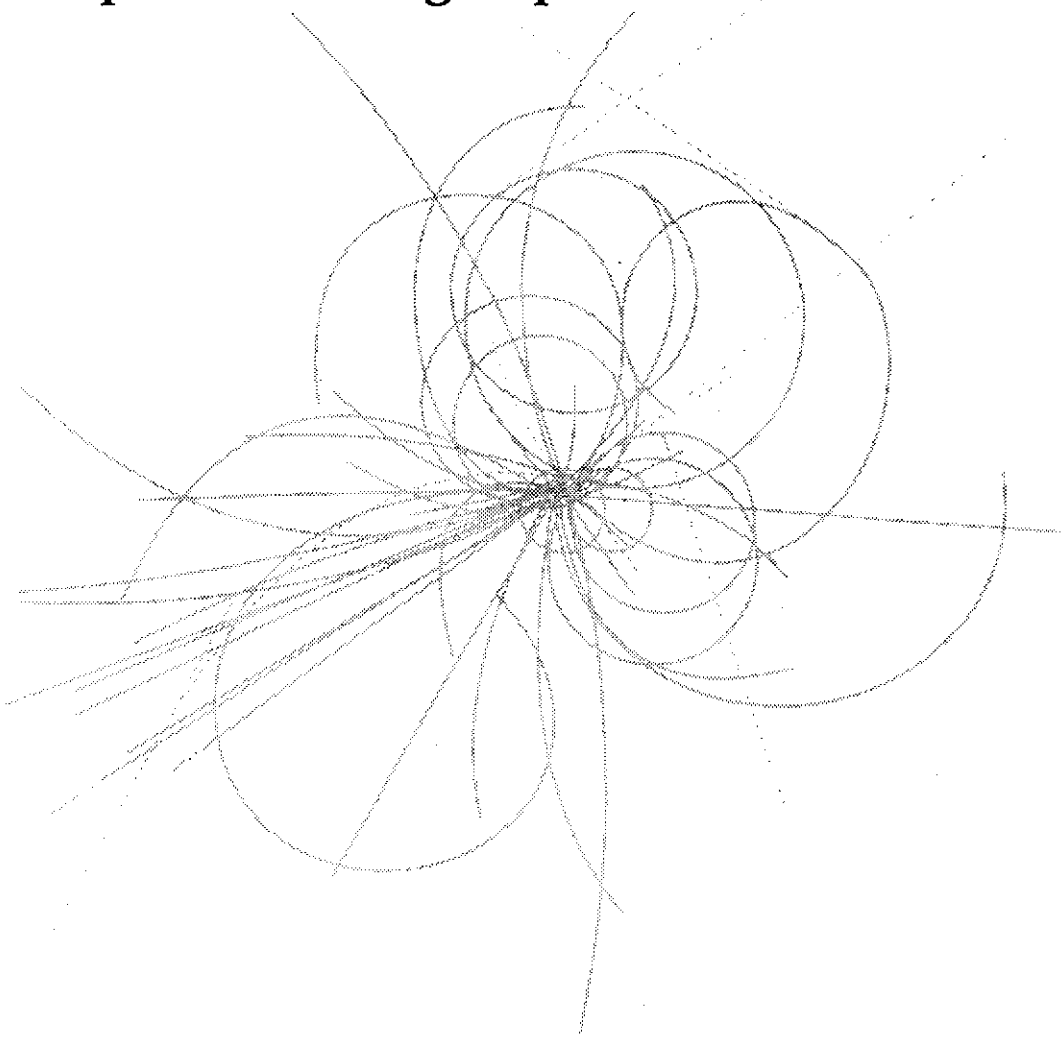

Papers Contributed to the 1992 Applied Superconductivity Conference

The Magnet Test Analysis Group

August 1992

SSCL-Preprint-147

Papers Contributed to the 1992 Applied Superconductivity Conference

The Magnet Test Analysis Group

Accelerator Design and Operations Division
Superconducting Super Collider Laboratory*
2550 Beckleymeade Ave.
Dallas, TX 75237

August 1992

*Operated by the Universities Research Association, Inc., for the U.S. Department of Energy under Contract No. DE-AC35-89ER40486.

Mechanical Performance of 5-cm-Aperture, 15-m-Long SSC Dipole Magnet Prototypes*

T. Ogitsu,[1,4] A. Akhmetov,[1] M. Anerella,[2] R. Bossert,[3] T. Bush,[1] D.W. Capone II,[1] J. Carson,[3] R. Coombes,[1] J. Cottingham,[2] S.W. Delchamps,[3] A. Devred,[1] J. DiMarco,[1] G. Ganetis,[2] M. Garber,[2] C. Goodzeit,[1] A. Ghosh,[2] S. Gourlay,[3] A. Greene,[2] R. Gupta,[2] R. Hanft,[3] A. Jain,[2] S. Kahn,[2] E. Kelly,[2] W. Koska,[3] M. Kuchnir,[3] J. Kuzminski,[1] M.J. Lamm,[3] P. Mantsch,[3] P.O. Mazur,[3] G. Morgan,[2] J. Muratore,[2] W. Nah,[1,5] D. Orris,[3] J. Ozelis,[3] T. Peterson,[3] E.G. Pewitt,[3] A. Prodell,[2] M. Puglisi,[1] P. Radusewicz,[1] M. Rehak,[2] E.P. Rohrer,[2] J. Royet,[6] W. Sampson,[2] P. Sanger,[1] R. Scanlan,[6] R. Schermer,[1] R. Shutt,[2] R. Stiening,[1] J. Strait,[3] C. Taylor,[6] R. Thomas,[2] P. Thompson,[2] J.C. Tompkins,[1] J. Turner,[1] M. Wake,[1,4] P. Wanderer,[2] E. Willen,[2] Y. Yu,[1] J. Zbasnik,[1] Y. Zhao,[1] and H. Zheng[1]

[1] Superconducting Super Collider Laboratory, Dallas, TX 75237 USA
[2] Brookhaven National Laboratory, Upton, NY 11973 USA
[3] Fermi National Accelerator Laboratory, Batavia, IL 60510 USA
[4] KEK, National Laboratory for High Energy Physics, Tsukuba, Ibaraki 305 Japan
[5] Korea Electrotechnology Research Institute, Changwon, Kyongnam 641-120, Korea
[6] Lawrence Berkeley Laboratory, Berkeley, CA 94720 USA

ABSTRACT

This paper summarizes the mechanical performance of the most recent 5-cm-aperture, 15-m-long SSC dipole magnet prototypes. The magnets were produced at Brookhaven National Laboratory (BNL) and Fermi National Accelerator Laboratory (FNAL) in cooperation with the Superconducting Super Collider Laboratory (SSCL). The BNL magnets rely on a horizontally-split yoke with collared ends, while the FNAL magnets rely on a vertically-split yoke with collet-style end clamps. Magnets of both designs are equipped with strain gauges enabling us to measure the azimuthal pressures exerted by the coils against the collar poles as well as the axial forces transmitted from the coil ends to the end plates. A comparison of the mechanical behaviors of the two magnet designs is presented. We also discuss how the behavior of the 5-cm-aperture magnets compares to that of the 4-cm-aperture prototypes.

INTRODUCTION

In January 1990, the decision was taken to increase the aperture of the SSC superconducting dipole magnets from 4 cm[1] to 5 cm.[2] A large effort was then undertaken at Brookhaven National Laboratory (BNL) and Fermi National Accelerator Laboratory (FNAL) in order to demonstrate the feasibility of the larger aperture magnets. Since then, seven 5-cm-aperture, 15-m-long dipole magnet prototypes have been produced and cold tested at BNL (magnets DCA207 through DCA213), while twelve more have been produced and cold tested at FNAL (magnets DCA311 through DCA322.) The production of the last FNAL magnet (DCA323) is now completed, and the magnet is awaiting its cold testing.

Seven of the FNAL-design magnets (magnets DCA313 through DCA319) were assembled at FNAL by personnel from General Dynamics (GD), and five of the BNL-design magnets (magnets DCA209 through DCA213) were assembled at BNL by personnel from Westinghouse Electric Corporation (WEC). These magnets were part of a technology transfer program from the National Laboratories to the dipole magnet contractors. Five of these industrially-assembled dipole magnet prototypes are used in a string test currently under way at SSCL.[3]

*Operated by the Universities Research Association, Inc., for the U.S. Department of Energy under Contract No. DE-AC02-89ER40486.

All the 5-cm-aperture, 15-m-long dipole magnet prototypes were cold-tested following the same generic test plan. The plan calls two testing cycles separated by a warm-up to room temperature. Each testing cycle includes quench tests, mechanical measurements, and magnetic measurements. Reference 4 presents a detailed review of the mechanical and quench performance of the early full-length prototypes (BNL magnets DCA207 through DCA209, and FNAL magnets DCA311 through DCA315). In this paper, we summarize the mechanical behavior during cooldown and energization of all the prototypes cold-tested so far. The quench performance of these magnets is discussed elsewhere.[5]

MAGNET FEATURES

The BNL and FNAL magnets are based on the same magnetic design,[6] and rely on the same concepts for their mechanical design.[4] The field is produced by a two-layer coil, which is mechanically restrained by means of laminated stainless steel collars. The collars are designed to provide a large azimuthal pre-compression to the coil in order to compensate the effects of the azimuthal component of the Lorentz force. The collared-coil assembly is encased in a laminated iron yoke, around which a stainless steel outer shell is welded. Yoke and shell are designed to tightly clamp the collared-coil assembly in order to stiffen the support against the radial and axial components of the Lorentz force. The main difference between the BNL and FNAL mechanical designs is in the way this clamping is realized. In the BNL design, the yoke is split horizontally and the clamping results from a positive collar-yoke interference along the vertical diameter. In the FNAL design, the yoke is split vertically, and the collar-yoke interference is along the horizontal diameter.

Other specific features of the BNL design include internal splices between the inner and outer conductors, located at the radius of the outer coil, and the fact that the coil ends are supported radially by collars similar to that of the magnet body. In the FNAL design, the splices are made at a radius larger than that of the outer coil, and the coil ends are supported by a four-piece G10 collet that is compressed radially by a tapered, aluminium cylinder. In both designs, the coil ends are loaded axially by four screws mounted into a

thick stainless end plate that is welded to the outer shell. Details of the features and construction of these magnets can be found in references 4, and 7 through 9.

For most of the prototypes, the cable insulation consists of a 25-μm-thick layer of Kapton, wrapped with a 50% overlap, completed by a 125-μm-thick layer of epoxy-impregnated fiberglass, wrapped with a 0.5-mm gap. The last two BNL magnets (DCA212 and DCA213), however, use a so-called *all-Kapton* insulation scheme, which consists of two layers of Kapton (30 μm and 34 μm in thickness, respectively), wrapped with a 50% overlap, and with a polyimide adhesive coating on the outer surface of the second layer. Similarly, the inner cable insulation of the last four FNAL magnets (DCA320 through DCA323) consists of two 25-μm-thick layers of Kapton, wrapped with a 50% overlap, while the outer cable insulation consists of a 25-μm-thick layer of kapton, wrapped with a 50% overlap, completed by a 25 μm-thick layer of Kapton, butt-wrapped with no overlap. For both the inner and outer coils of magnets DCA320 and DCA321, B-stage epoxy is coated on the outer surface of the second Kapton layer, while the second Kapton layer of magnets DCA322 and DCA323 is coated with Cryorad on both sides. Discrepancies in coil sizes resulting from the changes in cable insulation are compensated by adjusting the pole shim thickness (BNL magnets), or by installing brass shims next to the copper wedges and at the collar poles (FNAL magnets). The nominal curing temperature is 135 °C, except for magnets DCA212 and DCA213, which use 225 °C.

STRAIN GAUGE INSTRUMENTATION

The BNL and FNAL magnets are instrumented with two types of strain-gauge transducers:[10] 1) beam-type strain-gauge transducers, located at the collar poles and measuring the azimuthal pressures exerted by the coils, and 2) bullet-type strain-gauge transducers, located in the axial loading screws and measuring the force exerted by the coil against the end plates. The FNAL magnets have two strain-gauge collar packs, located respectively at the minimum and and the maximum of the azimuthal coil sizes, while the BNL magnets have only one, located at the minimum. (Each strain-gauge collar pack totals eight transducers.) Both ends of the BNL magnets are instrumented with bullet gauges, while only the non-lead end of the FNAL magnets is instrumented.

EXPECTED BEHAVIOR

During Cooldown

During cooldown, the various parts of the magnet shrink at different rates. In the azimuthal direction, the coil shrinks more than the Nitronic-40 stainless steel collars, resulting in a decrease of the pressure against the collar poles. On the 4-cm-aperture magnets, a clear correlation was established between the amplitude of the cooldown loss and the pressure at room temperature.[11] This was interpreted as an effect resulting from the non-linearity of the coil stress-strain curve: the higher the room temperature pre-compression, the stiffer the coil, and, for a given thermal shrinkage differential between the collars and the coil, the faster the rate of loss during cooldown.

In the radial direction, the Nitronic-40 stainless steel collars shrink more than the low carbon steel yoke. This results in a decrease of the collar-yoke interference along the axis where it is provided, while a gap develops or grows along the other axis. Table 1 summarizes the estimated collar-yoke interferences at room and liquid helium (LHe) temperatures for the nineteen prototypes discussed in this paper. For the BNL magnets, the numbers correspond to the interference along the vertical diameter, while, for the FNAL magnets, it corresponds to the horizontal diameter. The room-temperature values are based on actual measurements of the collared-coil assembly diameters, while the LHe-temperature values are deduced from the room-temperature estimates by taking into account the difference in thermal expansion coefficients between the collar and yoke steels. It appears that, for most of the BNL magnets, the collar-yoke interference is much smaller than that of the FNAL magnets.

In the axial direction, the outer stainless steel shell is expected to shrink more than the coil, thus resulting in an increase of the axial loading. In reality, however, the whole structure is tightly clamped radially, and axial motions of the cold mass components are restrained by friction. The end-force change during cooldown is thus somewhat unpredictable.

Table 1. Summary of collar-yoke interferences. (Warm and cold refer to room and LHe temperatures, respectively.)

BNL Magnets			FNAL Magnets		
Magnet	Interferences (μm)		Magnet	Interferences (μm)	
	Warm	Cold		Warm	Cold
DCA207	170	35	DCA311	330	195
DCA208	167	32	DCA312	340	205
DCA209	162	27	DCA313	335	200
DCA210	128	-7	DCA314	290	155
DCA211	186	50	DCA315	285	150
DCA212	175	39	DCA316	277	141
DCA213	226	90	DCA317	249	113
			DCA318	173	37
			DCA319	213	78
			DCA320	264	128
			DCA321	277	141
			DCA322	262	128

During Energization

The Lorentz force has three main components which are applied to the coil during energization: 1) an azimuthal component, which tends to compress the two coil layers towards the midplane and to unload the collar poles; 2) a radial component, which tends to bend the collars outwardly, with a maximum deflection at the midplane; and 3) an axial component, which tends to stretch the coil ends. During energization, the pressure against the collar pole is thus expected to decrease as a function of current squared, while the force against the end plate is expected to increase.

Furthermore, in the case of the BNL magnets, the cooldown shrinkage differentials result in a gap between the collared-coil assembly and the yoke along the horizontal diameter. During energization, the radial component of the Lorentz force thus

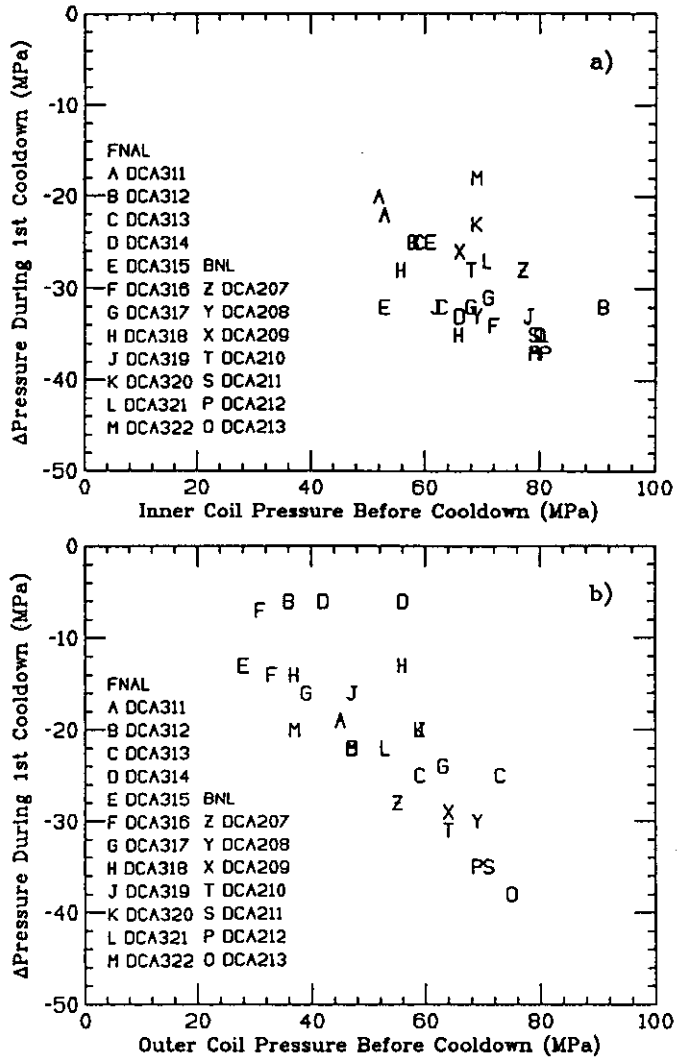

Fig. 1. Coil pressure change during cooldown vs. coil pressure at room temperature: a) inner layer, b) outer layer.

bends the collars and the coil deflects accordingly. This increase of the coil arc length results in a decrease of the coil pressure, thereby enhancing the unloading rate of the collar pole.[4,11] This unloading rate is also expected to be affected by the non-linearity of the coil stress-strain curve, and thus to depend on the level of pre-compression at zero current.

The axial component of the Lorentz force is estimated to be of the order of 2.1 kN/kA^2,[12] and distributes itself as a compressive load against the end plates and an extensive force on the coil body.[4,11]

COOLDOWN

Coil Pressure

Figure 1 summarizes the change in coil pressure during cooldown as a function of the coil pressure at room temperature for the nineteen magnets discussed in this paper. (For each strain gauge pack of each magnet, the pressures are averaged over the four quadrants of the given coil layer). As expected, the cooldown loss appears to increase quasi-linearly as a function of the room-temperature pressure, and the slope is similar for both inner and outer layers. Between 40 to 50 % of the room temperature pre-compression is lost during cooldown. Note that the all-Kapton insulation magnets behave similarly to the other magnets.

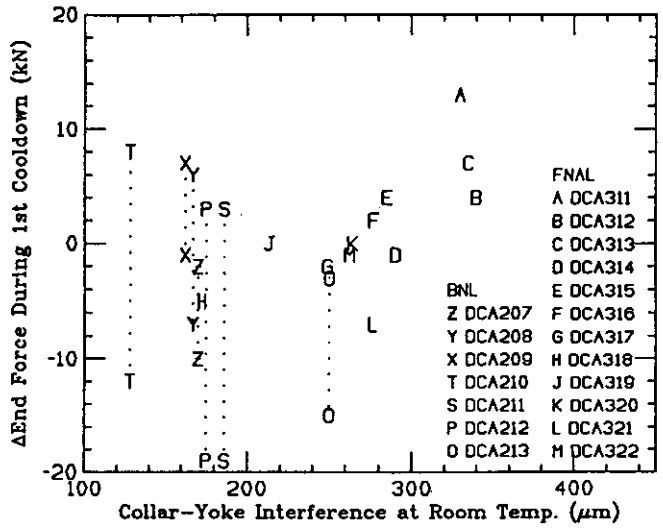

Fig. 2. End-force change during cooldown vs. warm collar-yoke interference. (For the BNL magnets, dotted lines connect the data from the two ends.)

End Force

One parameter determining the end-force change during cooldown is thought to be the collar-yoke interference at room temperature.[11] Figure 2 presents a summary of the end-force change during cooldown as a function of the estimated collar-yoke interference at room temperature. The data from the BNL magnets appear somewhat scattered, and there is a large difference between the lead end and the non-lead end of the magnets. The data from the FNAL magnets, however, appear more reproducible, and lie on a line with a positive slope. One explanation for this more reproducible behavior of the FNAL magnets may be that the larger collar-yoke interference forces collared-coil assembly, yoke, and shell to move more evenly during cooldown. The origin of the positive slope is not yet understood.

ENERGIZATION

Coil Pressure

Figure 3(a) presents a summary of the coil inner-layer pressure as a function of current squared for the BNL magnets, while Fig. 3(b) presents a similar plot for the FNAL magnets. The data displayed in Fig. 3 were taken during strain-gauge runs performed after the quench plateau had been established. For each magnet, the pressures are average over the four quadrants of a selected strain-gauge pack, and only current up-ramp data are displayed. For the BNL magnets, the unloading rates at low currents appear to be much faster than those of the FNAL magnets, while, at higher currents, the traces flatten and become nearly parallel to those of the FNAL magnets. Figures 4(a) and 4(b) present similar plots for the outer-layer pressure. The traces exhibit the same features as those in Fig. 3, except that the unloading rates are much slower. In addition, in Fig.

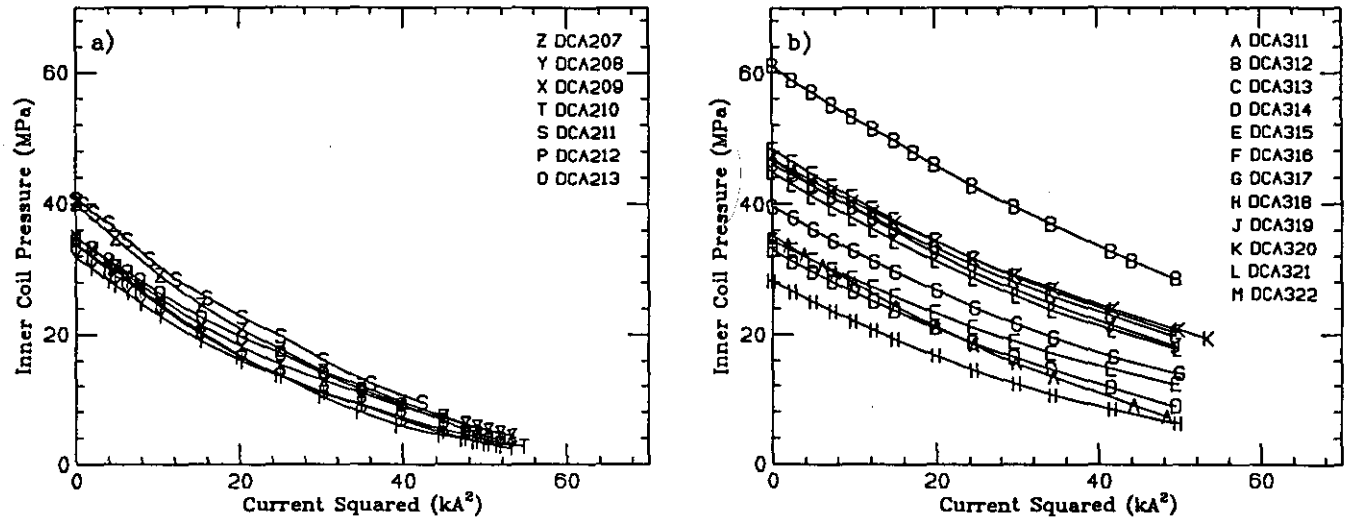

Fig. 3. Coil Inner-layer pressure versus current squared: a) BNL magnets, b) FNAL magnets.

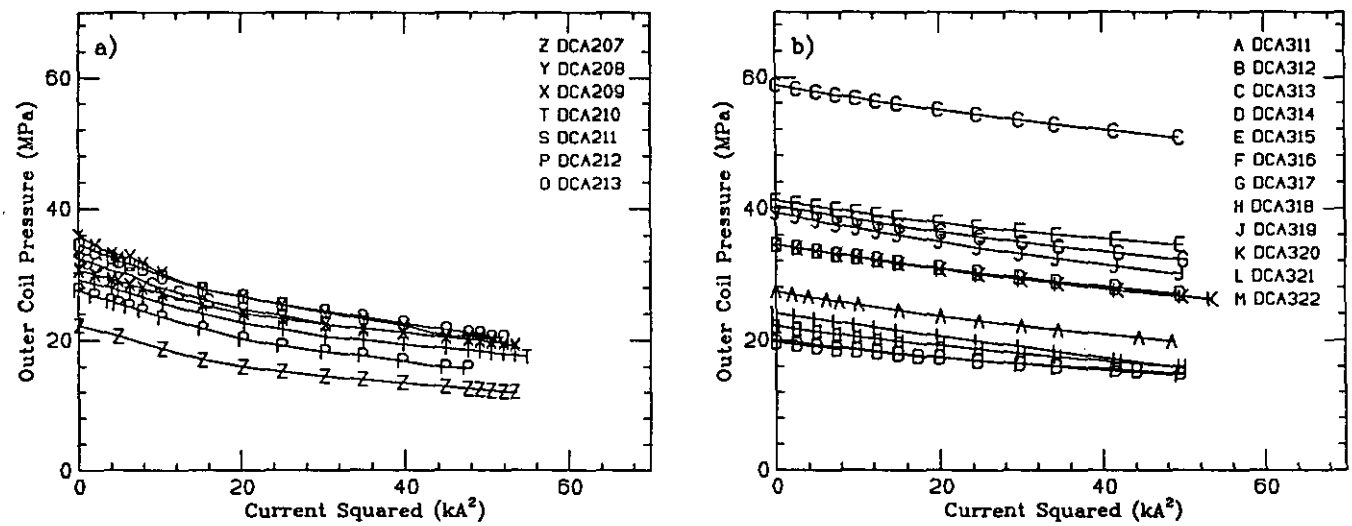

Fig. 4. Coil Outer-layer pressure versus current squared: a) BNL magnets, b) FNAL magnets.

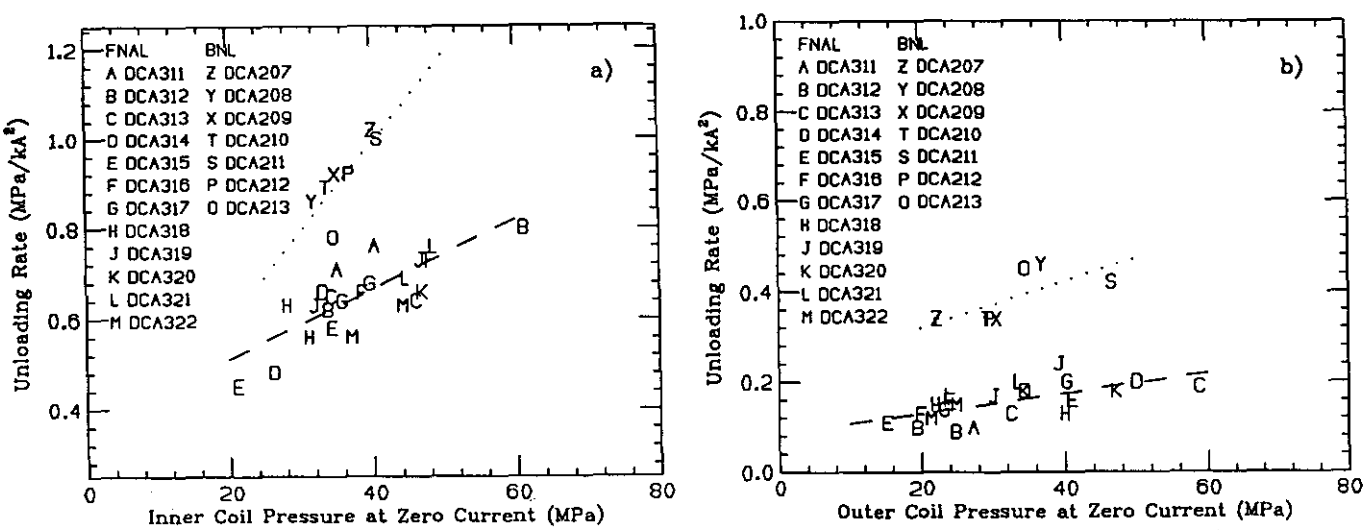

Fig. 5. Coil pressure unloading rate as a function of coil pressure at zero current: a) inner layer, b) outer layer.

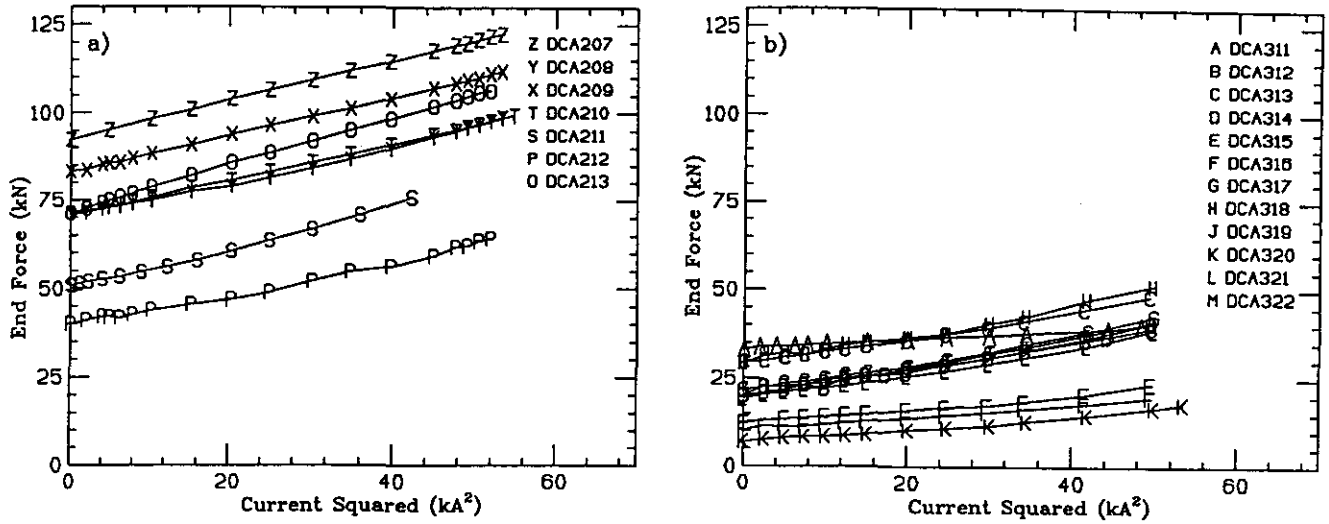

Fig. 6. Total end force versus current squared: a) BNL magnets, b) FNAL magnets.

4(a), the traces of the BNL magnets seem to exhibit a break at a current of about 4000 A. This breaking point is interpreted as the current at which the collared-coil assembly comes into contact with the yoke along the horizontal diameter.[4,11] For currents larger than the contact current, the BNL magnets behave similarly to the FNAL magnets. Note, once again, that the all-Kapton insulation magnets do not appear to behave differently from the other magnets.

As mentioned earlier, the initial unloading rate of the coil pressure is expected to depend on the coil pressure at zero current. Figure 5(a) presents a summary plot of the initial rate of unloading of the inner-layer pressure as a function of the pressure at zero current. The data clearly separate into two families, which correspond to the two magnet families. Furthermore, each of the families can be be fitted by a first order polynomial. Figure 5(b) presents a similar plot for the outer-layer pressure. Similarly to Fig. 5(a), the data separate into two families which can be fitted by a first order polynomial. In both figures, the dotted lines correspond to a linear fit of the BNL data, while the dashed lines correspond to a linear fit of the FNAL data. The dotted lines are always above the dashed lines and have steeper slopes.

Using a simple spring model,[13] the unloading rate of the coil pressure against collar pole can be predicted to be of the order of 0.55 MPa/kA^2 for both inner and outer layer. The unloading rates of the FNAL coil inner layers are consistent with this prediction. On the other hand, for the BNL magnets, the radial component of the Lorentz force causes the collars to bend outwardly, resulting in an increase of the arc length of the collar cavity, which enhances the coil pressure unloading rate. This explains why the dotted lines are above the dashed lines. Furthermore, as we also discussed above, the coil stress-strain curve is non-linear: the higher the pressure, the stiffer the coil. This explains why, although the Lorentz load is the same magnet-to-magnet, the four lines have a positive slope. Finally, since for the BNL magnets, the effects of the azimuthal component of the Lorentz force are combined with an increase of the arc length of the collar cavity, the effects of the non-linearity of the coil stress-strain curve are felt more severely. This explains why the dotted lines have steeper slopes that the dashed lines. The reason why the outer-layer unloading rates are much slower than the inner-layer ones is not clear. A possible explanation is that the radial pressure exerted by the inner layer restricts the unloading of the outer layer. Despite these slower rates, however, the amplitude of the difference between the BNL and FNAL magnets is of the same order of magnitude as that seen for the inner layer. This indicates that both layers of the coil have similar responses to collar deflections, which is consistent with what was observed for the cooldown data in Figs. 1(a) and 1(b).

End Force

Figure 6(a) presents a summary of the end force versus current squared for the the non-lead end of the BNL magnets, while Fig. 6(b) presents a similar plot for the FNAL magnets. The data displayed in Fig. 6 were taken during the same strain-gauge run as in Figs. 3 and 4, and correspond to the sum of the four bullet gauges. The end force loading rates of the FNAL magnets appear to be much smaller than that of the BNL magnets. This can be explained by the fact that the FNAL magnets have a larger collar-yoke interference, and that more of the axial component of the Lorentz force can be shared by friction between collared-coil assembly, yoke, and shell. (For the FNAL magnets, only 10 to 15% of the axial component of the Lorentz force is transmitted to the end plates.)

Figure 7 presents a summary plot of the initial loading rate of the end force as a function of the end force at zero current. Once again, the data appear to separate into two families, which correspond to the two magnet families. (One exception is FNAL magnet DCA311, which is known to have had yoke and end parts assembly problems.[4,14]). The dotted and dashed lines correspond to a linear fit of the BNL and FNAL data, respectively. The dashed line appears to have a steeper slope than that of the dotted line, possibly revealing that the collet-style FNAL ends have a more non-linear compliance than the simpler BNL ends.

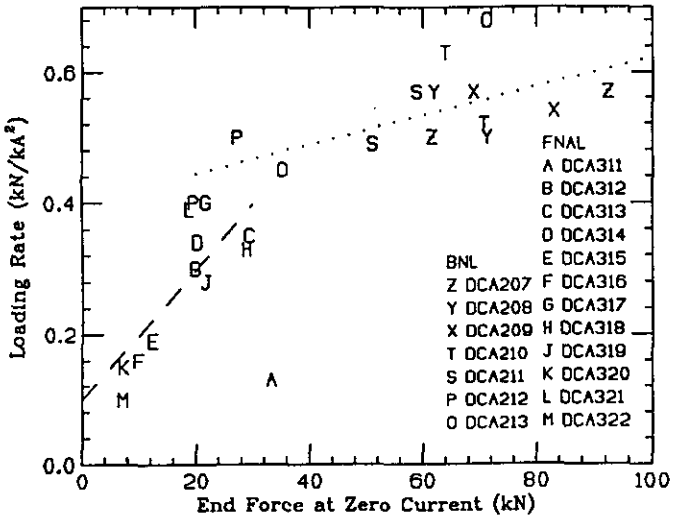

Fig. 7. End force loading rate versus end force at zero current.

As described in previous papers,[4,11] the BNL magnets exhibit a tendency to built-up end force in the course of their energization cycles. Table 2 presents a summary of end-force measurements after the first cooldown and before the first warm-up of the nineteen prototypes discussed in this paper. The end forces of the BNL magnets all appear to increase significantly duting cold-testing, while that of the FNAL magnets remain fairly constant. This end-force build-up, which mainly occurs at the time of the first excitations and quenches, is attributed to stick-slip motions of the collared-coil assembly within the yoke.

Table 2. Summary of end-force change during cold testing. (For the BNL magnets, the letters LE and NL refer to the Lead End and the Non-Lead End, respectively.)

BNL Magnets				FNAL Magnets			
Magnet	End Force (kN)			Magnet	End Force (kN)		
	Beg.	End	δ		Beg.	End	δ
DCA207LE	54	62	+8	DCA311	33	33	0
DCA207NL	66	90	+24	DCA312	18	20	+2
DCA208LE	51	59	+8	DCA313	29	29	0
DCA208NL	47	68	+11	DCA314	17	20	+3
DCA209LE	51	73	+22	DCA315	12	12	0
DCA209NL	27	88	+61	DCA316	9	11	+2
DCA210LE	33	65	+32	DCA317	20	32	+12
DCA210NL	58	72	+14	DCA318	26	n/a	n/a
DCA211LE	56	69	+13	DCA319	17	22	+5
DCA211NL	46	67	+21	DCA320	5	7	+2
DCA212LE	20	n/a	n/a	DCA321	16	19	+3
DCA212NL	5	n/a	n/a	DCA322	5	7	+2
DCA213LE	27	35	+13				
DCA213NL	25	70	+45				

CONCLUSION

The mechanical performance of the BNL and FNAL magnets correspond to their somewhat different designs, and no difference in behavior is observed between the various insulation schemes that were tried. A good qualitative understanding of the mechanical characteristic of these magnets was achieved. To carry out a more precise quantitative analysis, a finite element model including non-linear material properties at a level more advanced than is currently available would be required.

REFERENCES

[1] J.D. Jackson, ed., "Conceptual Design of the Superconducting Super Collider," SSC-SR-1020, March 1986; revised, September 1988.

[2] J.R. Sanford and D.M. Matthews, eds., "Site-Specific Conceptual Design of the Superconducting Super Collider," SSCL-SR-1056, July 1990.

[3] A.D. McInturf, J.G. Weisend II, *et al.*, "SSCL Half Cell Operational Test," in these Proceedings.

[4] A. Devred, T. Bush, *et al.*, "Review of SSC Dipole Magnet Mechanics and Quench Performance," to appear in *Supercollider 4*, J. Nonte, ed., 1992.

[5] W. Nah, A. Akhmetov, *et al.*, "Quench Performance of 5-cm-Aperture, 15-m-Long SSC Dipole Magnet Prototypes," in these Proceedings.

[6] R.C. Gupta, S.A. Kahn, and G.H. Morgan, "SSC 50 mm Dipole Cross Section," *Supercollider 3*, J. Nonte, ed., 1991, pp. 587-599.

[7] J. Strait, K. Coulter, *et al.*, "Experimental Evaluation of the Vertically versus Horizontally Split Yokes for SSC Dipole Magnets," *Supercollider 2*, M. McAshan, ed., 1990, pp. 731-741.

[8] M. Anerella, J. Cottingham, *et al.*, "Construction and Test Results from 15-m-Long, 50-mm-Aperture SSC Dipole," to appear in *Supercollider 4*, J. Nonte, ed., 1992.

[9] M.J. Blessing, D.E. Hoffman, *et al.*, "Construction Experience with Fermilab-Built Full-Length 50-mm SSC Dipole," to appear in *Supercollider 4*, J. Nonte, ed., 1992.

[10] C.L. Goodzeit, M.D. Anerella, *et al.*, "Measurement of Internal Forces in Superconducting Accelerator Magnets with Strain Gauges Transducers," *IEEE Trans. Magn.*, 25(2), 1989, pp. 1463-1468.

[11] A. Devred, T. Bush, *et al.*, "About the Mechanics of SSC Dipole Magnet Prototypes," AIP Conference Proceedings 249(2), 1992, pp. 1310-1374.

[12] D. Orrel, private communication.

[13] P Schmüser, "Superconducting Magnets for Particle Accelerators," AIP Conference Proceedings 249(2), 1992, pp. 1099-1158.

[14] M. Wake, M. Bleadon, *et al.*, "Mechanical Behavior of Fermilab/General Dynamics Built 15m SSC Dipoles," to appear in *Supercollider 4*, J. Nonte, ed., 1992.

Quench Characteristics of 5-cm-Aperture, 15-m-Long SSC Dipole Magnet Prototypes*

W. Nah,[1,5] A. Akhmetov,[1] M. Anerella,[2] R. Bossert,[3] T. Bush,[1] D.W. Capone II,[1] J. Carson,[3] R. Coombes,[1] J. Cottingham,[2] S.W. Delchamps,[3] A. Devred,[1] J. DiMarco,[1] G. Ganetis,[2] M. Garber,[2] C. Goodzeit,[1] A. Ghosh,[2] S. Gourlay,[3] A. Greene,[2] R. Gupta,[2] R. Hanft,[3] A. Jain,[2] S. Kahn,[2] E. Kelly,[2] W. Koska,[3] M. Kuchnir,[3] J. Kuzminski,[1] M.J. Lamm,[3] P. Mantsch,[3] P.O. Mazur,[3] G. Morgan,[2] J. Muratore,[2] T. Ogitsu,[1,4] D. Orris,[3] J. Ozelis,[3] T. Peterson,[3] E.G. Pewitt,[3] A. Prodell,[2] M. Puglisi,[1] P. Radusewicz,[1] M. Rehak,[2] E.P. Rohrer,[2] J. Royet,[6] W. Sampson,[2] P. Sanger,[1] R. Scanlan,[6] R. Schermer,[1] R. Shutt,[2] R. Stiening,[1] J. Strait,[3] C. Taylor,[6] R. Thomas,[2] P. Thompson,[2] J.C. Tompkins,[1] J. Turner,[1] M. Wake,[1,4] P. Wanderer,[2] E. Willen,[2] Y. Yu,[1] J. Zbasnik,[1] Y. Zhao,[1] and H. Zheng[1]

[1] Superconducting Super Collider Laboratory, Dallas, TX 75237 USA
[2] Brookhaven National Laboratory, Upton, NY 11973 USA
[3] Fermi National Accelerator Laboratory, Batavia, IL 60510 USA
[4] KEK, National Laboratory for High Energy Physics, Tsukuba, Ibaraki 305 Japan
[5] Korea Electrotechnology Research Institute, Changwon, Kyongnam 641-120, Korea
[6] Lawrence Berkeley Laboratory, Berkeley, CA 94720 USA

ABSTRACT

The quench performance and ramp rate sensitivity of eighteen 5-cm-aperture, 15-m-long SSC dipole magnet prototypes are discussed. All the magnets appear to reach a quench plateau near their extrapolated short sample current limit and well in excess of the operating current with very little training. Most of the magnets, however, exhibit a dramatic degradation of their quench current as a function of ramp rate, which for the most part, can be attributed to large cable eddy currents.

INTRODUCTION

Over the last year and half, eighteen 5-cm-aperture, 15-m-long SSC dipole magnet prototypes have been produced and cold-tested at Brookhaven National Laboratory (BNL) and Fermi National Accelerator Laboratory (FNAL) under contract with the Superconducting Supercollider Laboratory (SSCL). These magnets are part of an R&D program aimed at demonstrating the feasibility of the superconducting magnets for the SSC. They are also used to transfer technology from the National Laboratories to the dipole magnet contractors. Seven of the FNAL-design magnets (magnets DCA313 through DCA319) were assembled at FNAL by personnel from General Dynamics (GD), and five BNL-design magnets (magnets DCA209 through DCA213) were assembled at BNL by personnel from Westinghouse Electric Corporation (WEC). GD and WEC are respectively the leader and the follower of the collider dipole magnet contract. Five of these industrially-assembled dipole magnet prototypes, along with a quadrupole magnet prototype and a spool piece, were used in a string test recently performed at SSCL. There, the current was successfully ramped to 6520 A without any spontaneous quenching.[1]

The BNL and FNAL mechanical designs both rely on a tight clamping of the collared-coil assembly by the yoke in order to support the radial and axial components of the Lorentz force during energization, but they differ in the way this clamping is realized.[2] For the BNL magnets, the yoke is split horizontally and the clamping results from a positive collar-yoke interference along the vertical diameter, while, for the FNAL magnets, the yoke is split vertically and the clamping results from a positive collar-yoke interference along the horizontal diameter. Details on the design and mechanical performance of these magnets can be found in reference 3.

In this paper, we review the quench performance of the eighteen prototypes cold-tested so far, and we describe how it is affected by the current ramp rate.

QUENCH PERFORMANCE

Generic Test Sequence

With the exception of BNL magnets DCA208 and DCA211, all the magnets were tested following the same run plan. The run plan calls for two testing cycles, separated by a warm-up to room temperature. The first cycle includes quench testing at 4.35 K and ramp-rate study. The second cycle includes quench testing at 4.35 K, 3.85 K, and 3.5 K. Due to schedule constraints, magnet DCA208 was tested only at 4.35 K, while magnet DCA211 experienced an external bus failure during the first testing cycle. The bus is now repaired and the magnet is awaiting its second testing cycle.

BNL Magnets

Figure 1(a) presents a summary of the quench performance at 4.35 K of the BNL magnets. All the magnets reached 6600 A (the operating current of the SSC main ring) without quenching. Magnet DCA213 went directly to plateau, while the other magnets exhibited one or two training quenches. For magnets DCA207 and DCA208, the training quench currents were all above 7300 A. For magnets DCA209, DCA210, and DCA212, they were all above 7100 A. The lowest training quench is that of magnet DCA211 which occurred at 6692 A.

The determination of the training quench origins is complicated by the fact that some of them started between turn 1 and turn 13 of the inner coils, where there are no voltage taps (the turns are counted starting from the coil midplane). The second quench of magnet DCA207 originated at the lead end of lower inner coil turn 15 (the *lead end* is the magnet end where the current leads are located). The first and second

*This work is supported by the U.S. Department of Energy under Contract No. DE-AC35-89ER40486.

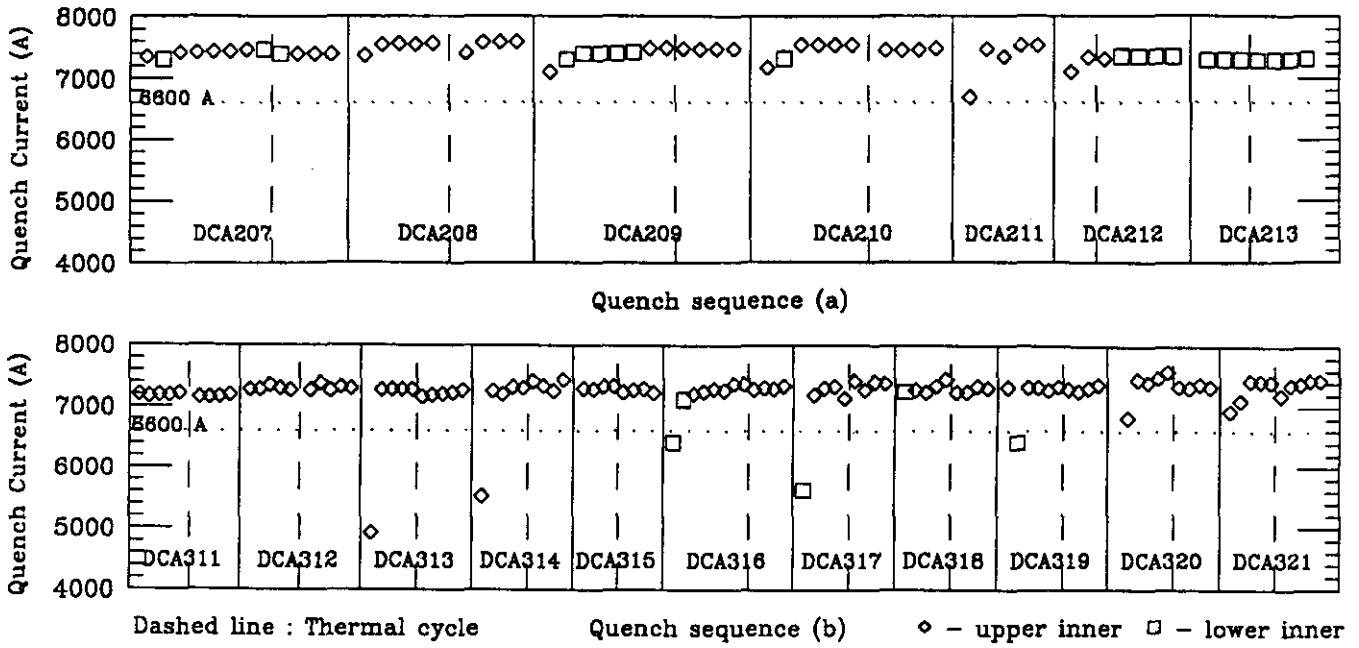

Figure. 1. Quench performance at 4.35 K of SSC dipole magnet prototypes: (a) BNL-design, and (b) FNAL-design magnets.

quenches of magnet DCA210, originated in the straight sections of upper inner coil turn 16 and lower inner coil turn 19. The first quench of magnet DCA212, originated at the non-lead end of upper inner coil turn 18. All the other training quenches originated in the multi-turn section.

All the plateau quenches started in the inner coil pole turn (turn 19), where the magnetic field is the largest. The plateau currents were all within 1% of the extrapolated short sample current limit. Note, however, the peculiar behavior of magnet DCA209. Quenches 1 to 6 were taken at 4 A/s (the nominal ramp rate of the SSC main ring), and they all originated between turn 1 and turn 13 of the inner coil. Starting with quench 7, the ramp rate was lowered to 1 A/s. As a result, the current went up by about 80 A, and the quench origin shifted to the inner coil pole turn. This extreme sensitivity on the ramp rate will be discussed in the next section.

The only magnet to exhibit re-training after a thermal cycle to room temperature was magnet DCA208, with a quench at 7407 A. The quench performance at low temperature was also quite satisfactory, with magnets DCA207 and DCA212 going directly to plateau at both 3.85 K and 3.5 K, and magnets DCA209, DCA210, and DCA213 requiring only one or two training quenches.

FNAL Magnets

Figure 1(b) presents a summary of the quench performance at 4.35 K of the FNAL magnets. Four of the magnets (magnets DCA313, DCA314, DCA316, and DCA317) exhibited a training quench below 6600 A. Magnets DCA320 and DCA321 also exhibited one or two training quenches, but they were all above 6600 A. The five remaining magnets reached a current very near the extrapolated short sample current limit on their first quench.

The low-current training quenches of magnets DCA313, DCA314, and DCA317 are very similar: they all originated toward the lead end of the inner coil pole turn, on the side opposite to the ramp-splice between the inner and outer coils. This axial location corresponds to the boundary between the last collar pack of the magnet body and the collet assembly that supports the coil end.[2] It also corresponds to the extremity of a G10 spacer, called the pole key, that supports the coil turnaround from the inside. The pole key, originally designed as a single piece, was, in these magnets, made of two pieces to facilitate assembly. It is believed that these three quenches resulted from movement of these various parts into a more stable position. After the first quenches, however, the three magnets went above 7250 A, and the problem did not resurface.

The first quench of magnet DCA316 was taken at 16 A/s and occurred at 6410 A between turn 1 and turn 13 of the inner coil. Subsequently, the magnet exhibited a behavior quite similar to that of BNL magnet DCA209. Quenches 4 to 6 were taken at 4 A/s and all originated between turn 1 and turn 13 of the inner coil. Starting with quench 7, the ramp rate was lowered to 1 A/s. As a result, the quench current went up by 100 A, and the quench origin shifted to the inner coil pole turn. Magnet DCA318 also exhibited an increase in quench current and a shift in quench localization when the ramp rate was lowered from 4 A/s (quenches 1 to 3) to 1 A/s (quenches after, and including, quench 4). The first quench of magnet DCA319 was close to the short sample current limit and originated in the inner coil pole turn, but its second quench occurred at 6415 A between turn 1 and turn 13 of the inner coil. Once again, this discrepancy can be related to a ramp-rate change: the first quench was approached at 1 A/s while the second quench occurred at 16 A/s. As we shall see in the next

section, BNL magnet DCA209 and FNAL magnets DCA316, DCA318, and DCA319 use inner cables made with strands coming from the same production batch of the same strand manufacturer.

As we already mentioned, the training quenches of magnets DCA320 and DCA321 were both above 6600 A. The first quenches of these two magnets originated between turn 1 and turn 13 of the inner coil (and were taken at 4 A/s), while the second quench of magnet DCA321 originated at the lead end of the upper inner coil pole turn (and was taken at 1 A/s).

The plateaus of the FNAL magnets appear somewhat less stable than those of the BNL magnets, but these fluctuations in the quench current result from temperature fluctuations. The only magnet to exhibit re-training after a thermal cycle to room temperature is magnet DCA321, with a quench at 7207 A. With the exception of magnet DCA314, all the magnets reached a plateau at both 3.85 K and 3.5 K in one or two training steps. Magnet DCA314 performed well at 3.85 K, but it did not sustain a stable plateau at 3.5 K.

RAMP RATE SENSITIVITY

When the current in a superconducting magnet is changed, heat is generated by several mechanisms: hysteresis in the superconductor and in the iron yoke, eddy currents flowing within individual cable strands, and eddy currents flowing from strand to strand. The resultant temperature increase causes a decrease in the plateau current of the magnet.

Figures 2(a) and 2(b) show the decrease in quench current versus ramp rate for selected BNL and FNAL magnet prototypes. The magnets in Figs. 2(a) and 2(b) have been grouped according to the manufacturer and the production batch of the strands used in their inner cables. It appears that, for the magnets of Fig. 2(a), the quench current remains roughly constant for ramp rates up to 25 A/s, above which, it starts to decrease quasi-linearly as a function of ramp rate. The worst case is magnet DCA312, which, at 200 A/s, quenches at about 2180 A, corresponding to 30% of its initial quench current. In comparison, the behavior of the magnets in Fig. 2(b) is quite different. The quench current starts by dropping significantly at low ramp rates, while the degradation at large ramp rates is much milder. The worst case is magnet DCA319, for which the quench current decreases from 7334 A at 1 A/s to 6156 A at 25 A/s, but is still of the order of 5000 A at 250 A/s. The magnets which are not included in Figs. 2(a) and 2(b) are using inner cables made with strands coming from different strand manufacturers or different production batches.

For all the magnets of Figs. 2(a) and 2(b), the plateau quenches at 1 A/s originated in the inner coil pole turn, where the field is the largest. For the magnets of Fig. 2(a), the quenches kept originating in the inner coil pole turn for ramp rates up to 25 A/s. For rates larger than 50 A/s, however, the quench origin shifted towards the inner coil midplane, between turn 1 and turn 13, where there are no voltage taps. On the other hand, for the magnets of Fig. 2(b), and as we described in the previous section, the shift in quench start localization from the inner coil pole turn to the multi-turn section occurred much sooner –between 1 A/s and 4 A/s– and was concomitant

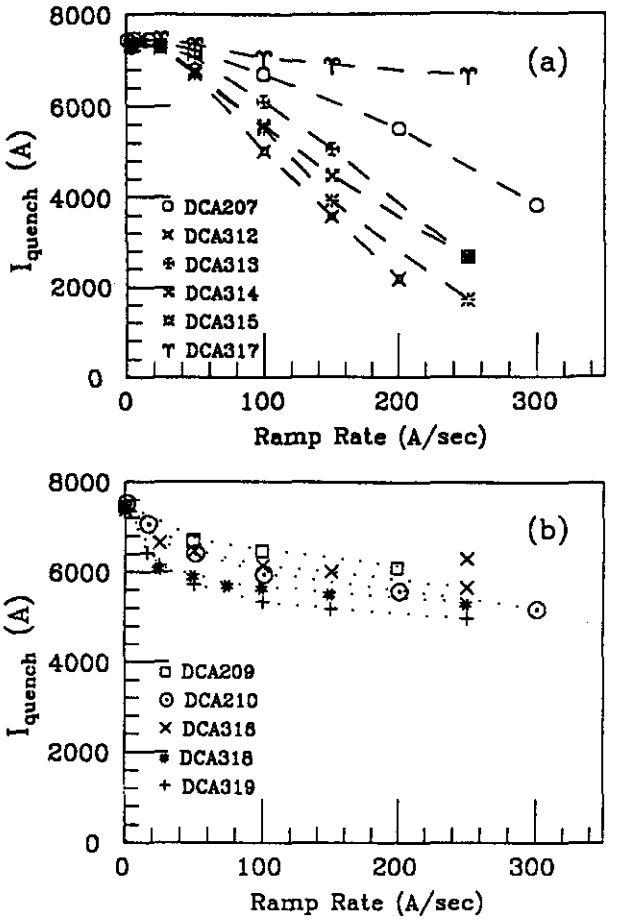

Figure 2. Ramp rate sensitivity of SSC dipole magnet prototypes. The magnets are grouped according to the manufacturer and the production batch of their inner cable strands.

to the sudden drop in quench current. Such a shift is consistent with what can be expected from the effects of cable eddy currents, which are larger towards the coil midplane, where the flux lines are perpendicular to the wide face of the cable.

In addition to quench testing at high ramp rates, AC-loss measurements were performed on most of the FNAL magnets[4] and on one of the BNL magnets (magnet DCA213).[5] The measurements were made electrically, using a simple sawtooth ramp between 500 A and 5000 A, with ramp rates varying from 30 to 150 A/s. For a given magnet, the energy loss per cycle appears to increase quasi-linearly as a function of ramp rate. Comparing the magnets with one another, it appears, that, for large ramp rates, there is a good correlation between the slope of the energy loss per cycle as a function of ramp rate and the slope of the quench current as a function of ramp rate. In other words, the magnets exhibiting the most dramatic quench degradation at large ramp rates are also the magnets exhibiting the largest AC losses. This consistency in the data indicates that both effects presumably result from the same cause, and that this cause is presumably cable eddy currents.

The next step is to try to determine the nature of these eddy currents. The inner (outer) cables used in SSC magnets consist of 30 (36) bare strands, twisted together, and shaped

into a flat, two-layer, slightly keystoned cable.[6] The cable mid-thickness is smaller than twice the strand diameter, and the contact surfaces at the crossovers between the strands of the two layers are relatively large. Also, during magnet assembly the coils are pre-compressed azimuthally.[3] Large pressures are thus applied perpendicularly to the cables, which keep the strands firmly in contact. The large contact surfaces and high pressures eventually result in low contact resistances at the strand crossovers, which couple the cable strands. Loops are thus formed where significant eddy currents can take place when subjected to a varying field.

Assuming that the eddy currents flowing from one strand to the other always pass through the crossover resistance, the cable can be represented as a simple model circuit.[7] Combining this model circuit with a two dimensional field calculation allows one to compute the cable eddy currents. The eddy-current loss can then be determined by integrating the power dissipated by the eddy currents in the crossover resistances.[8] Assuming that the crossover resistance, r_c, is uniform throughout the coil, the power, W, dissipated by the eddy currents over 1 m of SSC 5-cm-aperture dipole magnet can be estimated to be[9]

$$W = 2.5\times10^{-3}\,(dI/dt)^2/r_c \quad , \qquad (1)$$

where W is in W/m, r_c is in $\mu\Omega$, and $\partial I/\partial t$ is the ramp rate expressed in A/s. Hence, the total energy loss, E, over a 15-m-long magnet and a monopolar current cycle from 500 A to 5000 A to 500 A can be estimated to be

$$E = 340.\,(dI/dt)/r_c \quad , \qquad (2)$$

where E is in J/cycle.

Using Eq. (2) and the slopes of the energy loss per cycle as a function of ramp rate obtained experimentally, it is then possible to estimate the values of crossover resistances that are required to produce the observed effects. For the magnets of Fig. 2(a) on which AC loss measurements were performed (magnets DCA312, DCA314, and DCA315), the estimated crossover resistances are all below 10 $\mu\Omega$, while for the two magnets of Fig. 2(b) that were measured (magnets DCA318 and DCA319), r_c turns out to be of the order of 30 $\mu\Omega$.

Little is known on what determines the value of the crossover resistance in the case of bare-strand cables like the SSC cable. It is believed to depend on the thickness of the copper oxide layer that develops around the cable strands during the various steps of cable manufacturing and magnet assembly. A particularity of the SSC strands is that they are using high purity copper (RRR $\geq$ 300), and that they are not heat-treated after the final drawing. The RRR of the as-received cables are measured to be of the order of 30. During magnet assembly, the coils are cured for some length of time at temperatures in excess of 400 K and under pressures in excess 70 MPa. The RRR of the final coils are measured to be between 100 and 200. Speculations are that the curing cycle is accompanied by a strong annealing of the conductor, and that the parameters of this cycle strongly affects the development of the copper oxide layer. (It is also interesting to note that the only difference between magnet DCA317 and the other FNAL magnets of Fig. 2(a), is that it was collared twice, and that the delay between the coil curing and the final collaring was of the order of 120 days, compared to less than 50 days for the other magnets.)

The crossover resistance model seems to provide a reasonable basis for explaining the magnet behavior at large ramp rates. So far, however, we cannot explain the low ramp rate behavior of the magnets in Fig. 2(b), and why they behave differently from the magnets of Fig. 2(a).

The issue of ramp rate sensitivity is of particular relevance for the SSC High Energy Booster, which uses a nominal ramp rate of the order of 70 A/s. It is worth mentioning, however, that FNAL magnets DCA312, DCA313, DCA314, and DCA315 exhibited anomalous behavior of their magnetic field harmonics during current ramp at 4 A/s.[8,10] These anomalies, which cease when the current ramp is stopped, can also be explained in terms of eddy currents.[8]

CONCLUSION

The quench performance of the eighteen BNL-design and FNAL-design 5-cm-aperture, 15-m-long SSC dipole magnet prototypes cold-tested so far appears to be quite satisfactory, with only 4 training quenches below the operating current of the SSC main ring. Three of these four quenches are attributed to a design flaw in a coil end support piece, which has now been corrected. Magnets of the two designs, however, exhibit a dramatic decrease of their quench current as a function of ramp rate. This poor AC behavior can, for the most part, be attributed to large cable eddy currents. Efforts are now under way to confirm the nature of these eddy currents and determine the cable parameters that need to be mastered to control them.

REFERENCES

[1] A.D. McInturf, J.G. Weisend II, *et al.*, "SSCL Half Cell Operational Test," in these Proceedings.

[2] A. Devred, T. Bush, *et al.*, "Review of SSC Dipole Magnet Mechanics and Quench Performance," to appear in *Supercollider 4*, J. Nonte, ed., 1992.

[3] T. Ogitsu, A. Akhmetov, *et al.*, "Mechanical Performance of 5-cm-aperture, 15-m-long SSC dipole magnet prototypes," in these Proceedings.

[4] J. Ozelis, S.W. Delchamps, *et al.*, "AC Loss Measurements of Model and Full Size 50 mm SSC Collider Dipole Magnets at Fermilab," in these Proceedings.

[5] R. Thomas, private communication.

[6] D. Christopherson, D. Capone, *et al.*, "SSC 40mm Cable Results and 50mm Design Discussions," *IEEE Trans. Magn.* 27(2), 1991, pp. 1881-1883.

[7] G.H. Morgan, "Eddy Currents in Flat Metal Filled Superconducting Braids," *J. Appl. Phys.*, 44, 1973. p. 3319.

[8] T. Ogitsu, Y. Zhao, *et al.*, presented at the ICFA workshop on AC Superconductivity, KEK, National Laboratory for High Energy Physics, Tsukuba, Japan, June 23-25, 1992.

[9] T. Ogitsu, private communication.

[10] Y. Zhao, A. Akhmetov, *et al.*, "Current Dependence of Harmonic Field Coefficients of 5-cm-Aperture, 15-m-Long SSC Dipole Magnet Prototypes," in these Proceedings.

MECHANICAL PERFORMANCE OF FULL-SCALE PROTOTYPE QUADRUPOLE MAGNETS FOR THE SSC

J. M. Cortella£, A. Devred*, A. Wandesforde£

£Lawrence Berkeley Laboratory
1 Cyclotron Rd.
Berkeley, California 94720

*SSC Laboratory
2550 Beckleymeade Ave.
Dallas, Texas 75237

Abstract[1]--Six 5-m-long prototype quadrupole magnets have been built and cold-tested at Lawrence Berkeley Laboratory for the Superconducting Super Collider. Each of the magnets contained instrumentation to monitor the mechanical performance of the magnets during assembly and cold-testing. In addition, the instrumentation was used along with physical measurements as aids during magnet assembly. Quantities measured include coil pressures during assembly, cooldown, and magnet energization; axial thermal contraction of the magnets during cooldown; and axial force transmitted to the magnet end-plates. For the most part, mechanical measurements have proven repeatable and agree well with analysis.

I. INTRODUCTION

The Superconducting Super Collider (SSC) is designed to use approximately 1700 quadrupoles in its main ring for beam focusing [1]. These magnets are five meters in length and have an aperture of 4 cm. A cross-section of the magnet is shown in Figure 1. In the past two years, six full-scale prototype magnets have been built and tested at Lawrence Berkeley Laboratory to evaluate the baseline design as well as various features implemented during the program that were seen as improvements.

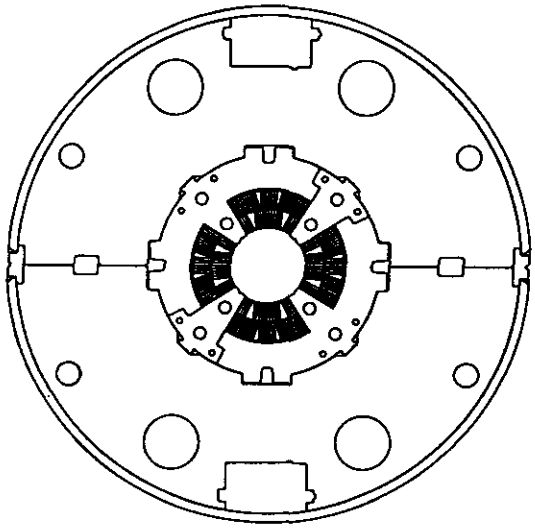

Fig. 1 - Two-dimensional cross-section of the SSC main ring quadrupole, showing all major components.

[1]This work was supported by the U.S. Department of Energy, under contract No. DE-AC35-89ER40486

This paper will report on the mechanical behavior of the magnets, focusing on measurements made during cold-testing. The primary parameters studied were coil pressures, endloads, and axial expansion of the magnets. More details on the construction of the magnets as well as the quench performance and magnetic field quality can be found in another paper [2].

II. INSTRUMENTATION

Each of the six magnets was extensively instrumented to measure quench detection, thermal behavior, and mechanical performance, but this paper will focus only on the instrumentation used to measure the mechanical performance of the magnets. Strain-gauge collar packs were used to measure coil pressures, axial compression load cells were utilized to measure axial loads on the ends of the magnets, and strain-gauge extensometers were utilized to measure the axial expansion and contraction of the outer shell of the magnet.

A. Strain-Gauge Collar Packs

Each of the magnets in the series was equipped with two strain-gauge collar packs. These are specially designed collar packs containing a bending-beam load cell adjacent to the pole turn of each coil [3]. A total of eight of these transducers are located within each collar pack, four used to measure the pressures on the inner coils and four used to measure the pressures on the outer coils. The strain gauges in each of the transducers are wired in a full-bridge to provide temperature and magnetic field compensation. The two gauge packs comprise a total of sixteen load cells within each magnet, providing coil pressure data during assembly, cooldown, and magnet energization.

B. End Load Cells

Compression-type load cells are placed on the endplates of the magnet to measure the changes in end compression during cooldown and energization. Each of the six magnets was instrumented with these load cells. However, on magnet QCC401 only those load cells placed on the "lead end" (the end from which the current leads extend) of the magnet were monitored due to a limitation in the data acquisition system. There are four of these load cells placed on either end, equally spaced around the periphery of the endplates [4]. Axial loads from the magnets are transferred through the load cells and reacted by the outer shell. As are the gauge packs, these load cells are also instrumented with a full strain gauge bridge.

C. Axial Extensometers

On magnets QCC402, QCC403, and QCC405, the contraction and expansion of the shell during cooldown and warm-up were measured. This was done using a long, thin stainless steel ribbon welded to the outer shell of the magnet. The ribbon was welded at the two ends of the strip so that it would move with the magnet shell. It was instrumented with strain gauges to provide a measurement of the thermal strain over the length of the shell, independent of local variations in shell stress. When the strip was attached to the shell, it was given a pre-tensile load to prevent buckling should the shell shrink more than the strip.

III. ASSEMBLY MEASUREMENTS

A. Coil Size

Each of the eight coils in any magnet was measured after curing. The azimuthal size of the coils was measured at ten axial positions along the length of the magnet while under pressures ranging from zero to 70 MPa. The measurements showed both systematic deviations, which were traced to variations in the curing cavity size, and random deviations, which were largest in the end regions. At the beginning of the program, there was a fairly wide spread in the coil sizes. The coils used in magnet QCC401 had deviations within a single coil on the order of 150μm, and coil-to-coil deviations of as much as 125μm. However, as experience was gained, both variations within a single coil and coil-to-coil deviations were reduced to less than 50μm for the inner coils and 75μm for the outer coils.

Coil size deviations can effect the final collared coil pressure significantly. Deviations on the order of 25μm result in changes in pressure on the order of 6.2 MPa using aluminum collars and 8.9 MPa using steel collars [5]. Thus, even with the small variations in coil size mentioned above, it is possible to develop a fairly large spread of pressures within a magnet. Therefore, during the assembly of a magnet, coils are sorted to match coil sizes so that quadrant to quadrant deviations are a minimum.

B. Collaring

After sizing and sorting, the eight coils are assembled around a mandrel and collared with interlocking, laminated collars. During the collaring operation, the gauge packs are first utilized as a means to monitor the effects of different size shims placed at the pole during "test collaring." The purpose of the test collaring is to determine the proper shim size that will provide the coils with a sufficient amount of coil compression, such that the coils remain in compression throughout the operation of a magnet. The pole shim size is uniform throughout the magnet, although one size is often used for the inner coils and a second size for the outer coils.

In collaring a magnet, the target coil pressure is approximately 40 MPa when a magnet is at 4.3 K and at zero current. Thus, in selecting a pressure at which to collar a magnet, it is necessary to compensate for any thermal contraction differences and loss in load due to creep of components. In addition, during the collaring operation, a hydraulic press is used to secure and compact the collars and coils so that the locking keys can be inserted without having to overcome large amounts of friction. The pressures on the coils during this operation are higher than the final collared pressure. Shown in Table 1 are the average peak stresses seen by the inner coils of each magnet, the final collared pressures, and the pressures just prior to the initial cooldown, showing the effects of creep. Cooldown effects will be discussed extensively in the next section.

Table 1 - Average Inner Coil Pressures During the Assembly of the QCC Quadrupoles (MPa)

	Peak Pressure	After Collaring	Prior to Cooldown
QCC401	-	39.1	36.8
QCC402	48.4	36.7	33.7
QCC403	54.1	41.7	39.8
QCC404	95.4	80.8	108.3
QCC405	120.2	75.6	68.2
QCC406	86.3	49.9	46.2

A number of salient points of Table 1 should be mentioned. First, the last three magnets were collared at higher pressures because they were constructed with stainless steel collars, which would result in thermal contraction changes greater than the first three magnets, as discussed in the next section. Also, for magnet QCC404 the pressure prior to cooldown is higher than the final collared pressure because this magnet was assembled with an interference between the collars and surrounding iron yoke, providing additional mechanical support. The increase represents the influence of the yoke at room temperature. Also, pressures greater than 80 MPa may not be very accurate, as the load cells are only calibrated to 80 MPa.

IV. COOLDOWN

During the cooldown of a magnet, differences in the thermal contraction properties of the magnet components lead to changes in the coil azimuthal stress as well as the axial loading. In this section, a summary of the cooldown changes in the coil pressures and endloads for each of the magnets is presented.

A. Prediction of Cooldown Changes in Coil Pressure

If the magnet is considered a uniform two-dimensional structure, it should be a simple matter to predict the changes in stress due to thermal contraction differences. For reference, only magnet QCC404 was designed to be supported by the yoke and outer shell. Also, a key design parameter of the magnets is the collar material. The first three magnets in the series used aluminum collars; the last three used Nitronic 40 stainless steel [2]. For the key materials used in this study, the thermal contraction coefficients between room temperature and liquid helium temperature are as follows [5]: aluminum, 4.0 mm/m; Nitronic 40 stainless steel, 3.0 mm/m; low-carbon steel, 2.0 mm/m; NbTi superconducting coil, 4.3 mm/m.

In addition to the differences in thermal expansion properties, there is another factor that must be considered in the prediction of a change in coil pre-compression. This being the fact that the conductor used in the SSC magnets has a distinct non-linear stress-strain behavior. This property complicates the prediction process considerably. The stress-strain behavior is very nearly parabolic, with an increasing modulus at higher stress levels. By fitting the curve with a parabolic equation, it is possible to analyze the effect this behavior has on the cooldown changes. An approximate relation for the stress-strain behavior of the coils is, from [6],

$$\sigma = A\varepsilon^2 + B\varepsilon + C \qquad (1)$$

with $A = 1.1 \times 10^6$ MPa, $B = -3400$ MPa, and $C = 8.0$ MPa.

The details of the prediction process can be found in [6], but the procedure essentially involves the computation of thermal contraction induced dimension changes in the coils, collars, and other major components. Then, using the length changes, one can compute the strain changes and resulting stress changes. After a bit of algebra and incorporating Eq. (1), the stress change from warm, σ_w, to cold, σ_c, is

$$\Delta\sigma = \sigma_w - \sigma_c = 2A\Delta\varepsilon^2 + (4A\varepsilon_w + B)\Delta\varepsilon. \qquad (2)$$

The above relation shows that the change in stress depends on the room temperature value of the strain. Thus, the greater the initial compression, the greater the pressure change during cooldown. In Eq. (2), the warm strain value is determined from the room temperature pressure value and Eq. (1).

B. Summary of Measured Cooldown Coil Pressure Changes

Plotted in Figure 2 are the predicted changes in stress for the quadrupole magnets for the different types of collar materials used, as well as the actual average cooldown losses from each of the six magnets tested. Each data point represents an average of the measurements from the four coils within a gauge pack. The test data and the analytical predictions both show that little change is expected in coil compression using aluminum collars; this because the coils and aluminum have similar thermal contraction properties. Thus, the use of aluminum collars allows one to assemble a magnet at lower initial pressures than a steel collared magnet, but still retain sufficient coil compression when cold.

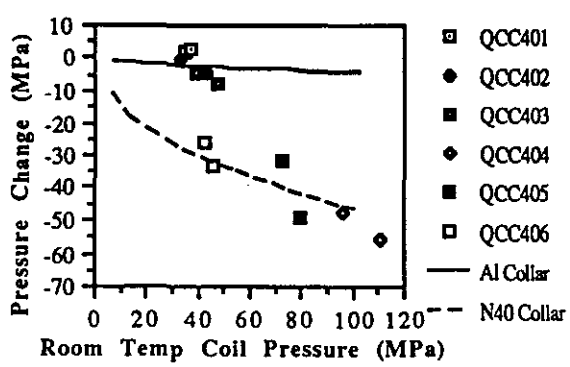

Fig. 2 - Plot of cooldown changes in coil pressure along with predicted relations for each of the six SSC quadrupoles tested.

One further aspect of the data in Fig. 2 needs to be considered as well. As mentioned earlier, magnet QCC404 utilized the yoke for support. It was built with a nominal interference of 100μm between the collars and the yoke. As the steel collars shrink away from the yoke, one expects an added loss in compression as a result of the release of stored elastic energy. This should result in greater cooldown changes than the non-supported magnets. However, as shown in Fig. 2, QCC404 seems to behave the same as the other steel-collared magnets. The reason for this apparent discrepancy is not fully understood. More data on yoke-supported magnets would be necessary to make any conclusions regarding the behavior of yoke-supported magnets.

C. Prediction of Endload Change During Cooldown

The primary means of end support was the use of a one-inch-thick steel endplate butted up against the end of the coils. However, in some magnets, additional support was used. In magnets QCC402, QCC404, QCC405, and QCC406 an additional ring was clamped around the coils 15 cm away from either end. The ring clamp was then bolted to the last yoke block, which is physically mated to the shell via a large frictional force as a result of weld shrinkage. Thus, the coils, yoke, and shells are all tied together; the idea being that they would all move together during any axial expansion or contraction.

The manner in which a magnet was supported axially had a pronounced effect on the change in axial load during cooldown. In the magnets with the bolted-ring clamp, the changes in endload observed are a result of changes within the end region of the magnet only, since the straight section of the magnet is locked to the shell. The changes observed are a function of the thermal contraction differences of the aluminum end clamp and the stainless steel shell as well as the relative stiffness of magnet components in the end region. These length contractions along with calculated stiffnesses can provide a prediction for the cooldown loss following Hooke's Law. The calculated stiffness of the end region, with the aluminum end clamp and the coil end acting as two springs in parallel with the endplate acting as a spring in series, would be

$$k_{eq} = \frac{k_1(k_2 + k_3)}{k_1 + k_2 + k_3} \qquad (3)$$

where k_1 = stiffness of endplate = 1.2×10^5 kN/m from [7]

k_2 = stiffness of coil end

$= \left(\frac{AE}{L}\right)_{end} = 3.4 \times 10^5$ kN/m

k_3 = stiffness of aluminum end clamp

$= \left(\frac{AE}{L}\right)_{alum} = 5.1 \times 10^5$ kN/m.

In the above,

A = the area of the coil end or aluminum clamp (m^2)

E = the elastic modulus of the coil end, assumed to be dominated by the G-10 end spacers, or aluminum end clamp (MPa)

L = the length of the region between the endplate and the bolted-on ring clamp (15cm).

This results in an equivalent stiffness of 1.1×10^5 kN/m, which agrees fairly well with an experimentally measured value of 9.2×10^4 kN/m. Based on a change in length determined by the thermal contraction difference between the aluminum endclamp and the stainless steel shell during cooldown (1 mm/m), the loss in axial compression in the last 15 cm should be approximately

$$F = k_{eq}\Delta x = 1.1 \times 10^5 \text{ kN/m}[(.001\text{m/m})]0.15\text{m} = 16.5 \text{ kN}.$$

D. Summary of Measured Endload Changes During Cooldown

Listed in Table 2 is a summary of the endload changes during cooldown for each of the six magnets in this study. Although the scatter in the data is fairly large, average load changes agree well with prediction for the four magnets that used the end clamp, locking the straight section of the magnet to the shell.

Table 2 - Changes in Endplate Load for Six SSC Quadrupoles During Cooldown (kN)

	Lead Endplate	Return Endplate
QCC401	5.0	-
QCC402	14.7	14.6
QCC403	51.7	50.1
QCC404	11.6	14.7
QCC405	9.2	24.1
QCC406	21.4	19.3

The load change in QCC401 is low by comparison. Magnet QCC401 did not utilize a bolted-ring end clamp, and therefore, the region which was affected by thermal contraction differences included a significant portion of the straight section of the coils. In this situation, the end region is much less stiff, and the differences between the thermal contraction of the stainless steel shell and the aluminum end clamp have little effect in changing the load.

The endload change in QCC403 is notably high. This is a result of a modification in design compared to the other magnets. In all magnets except QCC403, the endplate contacted solely the end of the coils and not the much larger diameter aluminum end clamp surrounding the coil ends. However, in magnet QCC403 additional shims were placed between the endplate and the large aluminum end clamp, distributing the load over a much wider area. This effectively increased the stiffness of the end region by a factor of three, and the load changes during cooldown seem to be a response to this design change.

E. Axial Expansion

The axial extensometer strips which were placed on the outer diameter of the shell were made of stainless steel, as was the shell itself. Therefore, any apparent strain measured on the gauges would be due to *differences* in thermal contraction between stainless steel strip and the shell. The shell has a greater coefficient of thermal expansion than does the yoke around which it is welded. Therefore, as the shell shrinks around the yoke, azimuthal stress will increase. This increase in azimuthal stress translates to an increase in the axial strain as dictated by Poisson's ratio, which is 0.3 for steels.

In each of the magnets on which the axial expansion strips were used, an apparent change in strain of approximately 0.2 millistrain was measured. If the shell were free to expand and contract longitudinally, the axial strain that would be expected would be simply Poisson's ratio multiplied by the azimuthal strain. Given that the difference in thermal expansion between the stainless steel shell and the iron yoke from room temperature to liquid helium is 0.9mm/m, the expected axial strain would be 0.27 millistrain.

A possible explanation for the difference between the 0.2 value measured and the theoretical value of 0.27 is because the shell is not free to contract axially. The iron yoke is placed on the magnet in eighteen-inch-long sections known as yoke packs. These packs are placed on the magnet by hand, and small gaps are left between each pair of yoke blocks. As the magnet cools, these blocks are pulled together by the shell, and the gaps eventually close. Once the gaps are closed, the shell is no longer free to contract; it behaves as the yoke blocks do. Thus, the overall axial contraction is less than what it would be had the shell been completely free to contract.

V. ENERGIZATION

A. Prediction of Coil Unloading During Energization

During energization of a magnet, the Lorentz forces acting upon a coil result in a redistribution of stress within the coils. These forces are proportional to the product of the magnetic field and the current in the coils. In addition, the field is proportional to the current as well. Therefore, it follows that the Lorentz forces are proportional to the square of the current. Thus, all plots and data comparisons will discuss the behavior of the energization loads as a function of current squared.

Analytical computations used to predict the degree of the coil unloading during energization give a value of approximately 0.21MPa/kA^2 for both the inner and outer coil [8]. These models use a constant elastic modulus to represent the behavior of the coils, and computations provide an "energization response" which is independent of initial values. Therefore, at the operating current of the SSC, 6500A, the coils should lose approximately 8.9 MPa.

B. Summary of Coil Pressure Changes During Energization

Shown in Figure 3 is a typical trace of the inner coil pressures during the energization of a magnet as a function of the current squared. The data is from magnet QCC404. The data represent the coil pressures from each of the four quadrants in the gauge pack nearest the end of the magnet with the current leads. The labels in the legend represent the individual load cell identification numbers, with the number corresponding to the respective quadrant.

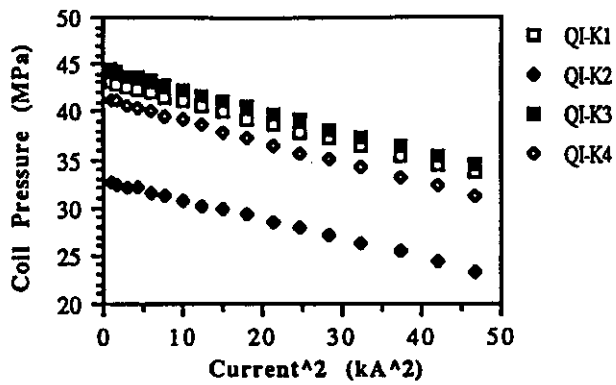

Fig. 3 - Trace of inner coil pressures during the energization of magnet QCC404 at 4K.

As with the coil pressure changes during cooldown, the changes during energization also were a function of the initial pressure level. The higher the initial pressure, the greater the magnitude of the slope. For the traces shown, the slopes vary from 0.25 MPa/kA^2 for the trace starting at 33 MPa to 0.35 MPa/kA^2 for the curve with an initial value of 45 MPa.

The dependence of the slope on the initial pressure is again a product of the non-linear elastic properties of the conductor, as discussed earlier. If the slopes of each of the individual load cell signals are plotted as a function of the initial pressure on the magnet, then a definite relation develops. Figure 4 presents such data. It displays the average of the inner coil slopes from each gauge pack for each of the six magnets tested. Therefore, the analytical prediction developed with finite elements using linear elastic coil properties mentioned earlier is not very accurate. Actual values may differ from the predicted value by as much as a factor of two.

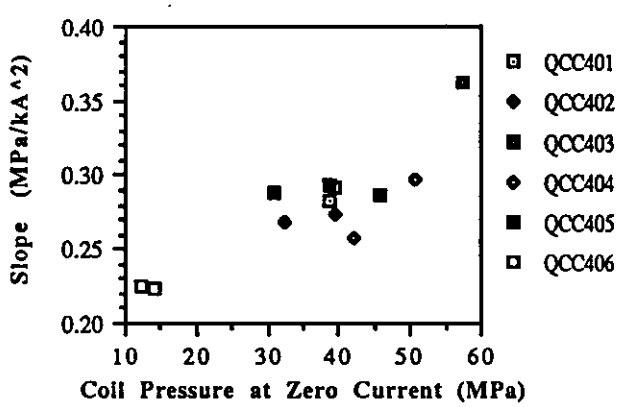

Fig. 4 - Dependence of energization response of the inner coils on initial pressure level.

In addition, there are other influences that affect the changes during energization. It was discovered that a magnet responds differently on its first energization than it does during subsequent energizations. Shown in Figure 5 is a trace of two load cells from the first energization of magnet QCC406. The magnet was cycled between 0A and 5000A three times and then ramped to quench. The coil pressures do not return to their original zero current values after the initial energization to 5000A. In addition, there is a decrease in the slope of the traces, all of which indicates that the coils have been compacted into a slightly tighter, stiffer package after being subjected to the Lorentz loading. These changes in the slopes and shifting of zero current pressure levels indicate that the Lorentz load tends to reposition the coils into a "favorable" position.

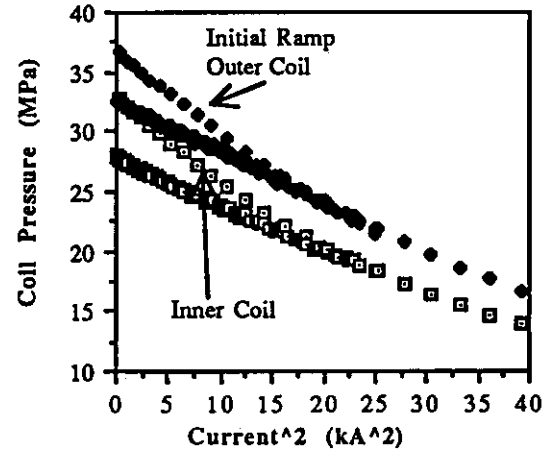

Fig. 5 - Comparison of initial and subsequent rampings of a magnet, showing changes in coil pressure. Data is from first training of magnet QCC406.

C. Effects of a Thermal Cycle on Coil Pressures

The changes in energization response of the coils are obviously more than a by-product of the materials properties of the conductor or other components, since the response changes once the magnet reaches a new current level. It appears that there is a frictional force that locks the coil in a new position once it has been energized beyond a certain force level. This locking into place may be a key to training. There is a stable position within the magnet that allows it to reach a plateau current comparable to the critical current. Unfortunately, in order for the conductor to move into this favorable position, it must overcome friction, resulting in small amounts of heat generation which force the conductor into a normal state, and quenching occurs. Each of the quadrupoles tested have had a significant number of training quenches, although the number has decreased with the later magnets [2].

An important question is whether or not the changes in mechanical behavior that took place during the initial training remain once a magnet has been warmed to room temperature and re-cooled. If the behavior shown in Fig. 5 does not manifest itself during the second training cycle, then one might say that the magnet "remembered" its initial training, and its quench performance should improve. Unfortunately, subsequent cold-testing of magnets have always shown very repeatable behavior. Coil pressure traces versus current squared from the first quench after a magnet has been warmed and cooled a second time are essentially identical to the original tests.

Other evidence of the magnets' inability to remember its training is illustrated in "history" plots of the coil pressure. They show that the sums of the coil pressure changes during

cooldown and the zero current shifts that take place during cold-testing are equal to the coil pressure changes during warm-up. Figure 6 plots the history of the average coil pressures within each gauge pack of magnet QCC403. The labels on the horizontal axis refer to subsequent steps in the testing of a magnet, from just prior to the initial cooldown to the final room temperature reading. The "cold" label refers to the coil pressure taken once the magnet has reached liquid helium temperature but prior to any energization of a magnet. The "plateau" label refers to coil pressures at zero current taken once a magnet has been repeatedly quenched. The figure shows that the magnet "forgets" its training. That is, after a thermal cycle, the magnet returns to its initial state, and when cooled a second time, it returns to its pre-energized state.

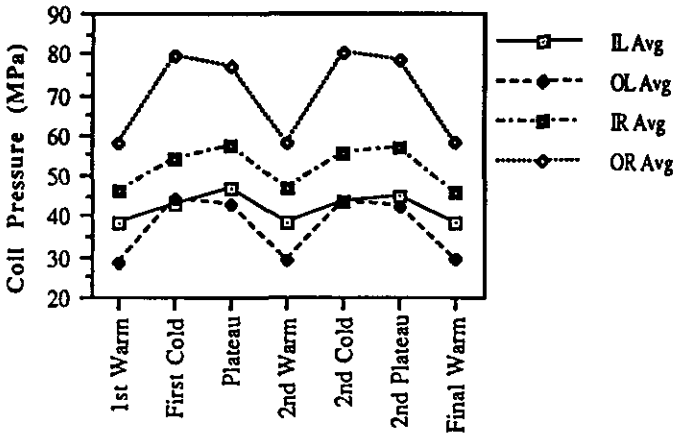

Fig. 6 - History of inner coil load cells during various phases of cold-testing of magnet QCC403. In the legend, I represents inner coil; O, outer coil; L, lead end pack; and R, return end pack.

D. Endload Behavior During Energization

Four of the six magnets tested used an end design that locked all but the last 15 cm of the coils to the shell. Therefore, the endload changes during energization are primarily a product of the relative motions in the very end region of the magnets, the last 15 cm or so between the endplates and the bolted-ring clamp used in all magnets except QCC401 and QCC403. The total axial Lorentz load has been calculated to be 24.5 kN [8], pulling the ends of the coils outward. Table 3 lists the slopes of the endload versus current squared traces and the percentage of predicted. The difference in the measured and the predicted values is due to the stiffness of the coils and the mechanisms used to transfer load directly to the outside skin.

Table 3 - Endload Responses of QCC Quadrupoles

	Response (kN/kA^2)	% of Total Predicted
QCC401	0.28	48.0
QCC402	0.068	11.7
QCC403	0.258	44.5
QCC404	0.036	6.2
QCC405	0.034	5.8
QCC406	0.027	4.7

The effect of the bolted-ring end clamp is clearly illustrated, with as little as 5% of the axial Lorentz load being transferred to the endplates. As mentioned earlier, these rings were employed so that the collared coil, yoke blocks and skin would all move together in the axial direction. The measured responses are largely a result of motions only in the very end region of the coils.

However, with magnets QCC401 and QCC403, the only way axial Lorentz load could be transferred to the shell without appearing at the endplate was through collar-yoke friction. Since the yoke was not intended to support the collars in these magnets, the response values are considerably higher than for other magnets that used the bolted-on end clamp.

VI. SUMMARY

The six prototype SSC main ring quadrupoles have shown repeatable mechanical performance. Instruments developed to monitor mechanical behavior have provided information on the behavior of the magnets during assembly, cooldown, and energization. The instruments developed were used to monitor coil pressures, endloads, and axial expansion of the magnets. During assembly, the instrumentation was a useful assembly aid. Measurements have shown that the magnets' behavior during cooldown is as predicted, but depends highly on the non-linear material properties of the conductor. From cold-testing, the primary result from the measurements is the demonstration of the inability of these magnets to "remember" their initial training. It has been demonstrated that Lorentz loading of a magnet changes the mechanical behavior of the magnets. But, upon having been warmed to room temperature, cooled, and then retested, their mechanical behavior is nearly identical to that during the initial energization. Axial contraction data and endload behavior are consistent with design features of each magnet.

REFERENCES

[1] J.R. Sanford, D.M. Matthews, eds., "Site Specific Conceptual Design for the Superconducting Super Collider," SSCL-SR-1056, July, 1990.

[2] A. Lietzke, C. E. Taylor, et al "Construction and Test Results of 40 mm Bore 5m Long Quadrupole Magnets for the SSC," Paper LN-4, In these proceedings.

[3] A. Wandesforde, "Load Cell Pack for LBL SSC Quadrupole Prototypes," LBL-DWG-23F6806. 1990.

[4] J.M. Cortella, "Axial Load Measurements on Superconducting Magnets," SC-MAG-357, 1991.

[5] J.M. Cortella, "Preliminary Study of the Mechanical Performance of SSC Quadrupole Magnets," LBL Report SC-MAG-368, 1992.

[6] A. Devred, et al, "About the Mechanics of SSC Dipole Magnet Prototypes." AIP Conference Proceedings, Vol. 249 (2), 1992, pp. 1309-1374.

[7] Roark and Young. *Formulas for Stress and Strain*, 5th ed. McGraw-Hill, New York, 1975.

[8] D. Dell'Orco, "Finite Element Analysis of the QC Quadrupole for the SSC," LBL Report SSC-MAG-260.

[9] S. Caspi, Private communication.

Current Dependence of Harmonic Field Coefficients of 5-cm-Aperture, 15-m-Long SSC Dipole Magnet Prototypes*

Y. Zhao,[1] A. Akhmetov,[1] M. Anerella,[2] R. Bossert,[3] T. Bush,[1] D.W. Capone II,[1] J. Carson,[3] R. Coombes,[1] J. Cottingham,[2] S.W. Delchamps,[3] A. Devred,[1] J. DiMarco,[1] G. Ganetis,[2] M. Garber,[2] C. Goodzeit,[1] A. Ghosh,[2] S. Gourlay,[3] A. Greene,[2] R. Gupta,[2] R. Hanft,[3] A. Jain,[2] S. Kahn,[2] E. Kelly,[2] W. Koska,[3] M. Kuchnir,[3] J. Kuzminski,[1] M.J. Lamm,[3] P. Mantsch,[3] P.O. Mazur,[3] G. Morgan,[2] J. Muratore,[2] W. Nah,[1,5] T. Ogitsu,[1,4] D. Orris,[3] J. Ozelis,[3] T. Peterson,[3] E.G. Pewitt,[3] A. Prodell,[2] M. Puglisi,[1] P. Radusewicz,[1] M. Rehak,[2] E.P. Rohrer,[2] J. Royet,[6] W. Sampson,[2] P. Sanger,[1] R. Scanlan,[6] R. Schermer,[1] R. Shutt,[2] R. Stiening,[1] J. Strait,[3] C. Taylor,[6] R. Thomas,[2] P. Thompson,[2] J.C. Tompkins,[1] J. Turner,[1] M. Wake,[1,4] P. Wanderer,[2] E. Willen,[2] Y. Yu,[1] J. Zbasnik,[1] and H. Zheng[1]

[1] Superconducting Super Collider Laboratory, Dallas, TX 75237 USA
[2] Brookhaven National Laboratory, Upton, NY 11973 USA
[3] Fermi National Accelerator Laboratory, Batavia, IL 60510 USA
[4] KEK, National Laboratory for High Energy Physics, Tsukuba, Ibaraki 305 Japan
[5] Korea Electrotechnology Research Institute, Changwon, Kyongnam 641-120, Korea
[6] Lawrence Berkeley Laboratory, Berkeley, CA 94720 USA

ABSTRACT

Eighteen 5-cm-aperture, 15-m-long SSC dipole magnet prototypes have been produced and cold tested. On each prototype, the dependence of harmonic field coefficients on magnet current was measured as part of a study of the magnetic field quality. For most of the magnets, the observed behavior conforms to what can be expected from the effects of persistent magnetization currents and iron yoke saturation. A few prototypes, however, exhibited anomalies during current ramp at 4 A/s which can be attributed to large cable eddy currents.

INTRODUCTION

The field produced by superconducting magnets has mainly three components: 1) a component, B_t, resulting from the transport current, I, circulating in the coil, 2) a component, B_m, resulting from persistent magnetization currents circulating in the superconducting filaments, and 3) a component, B_e, resulting from cable eddy currents. The B_t component only depends on the coil geometry and is expected to vary linearly as a function of I. The B_m component is dominated by the critical current density of the superconductor, which depends on the temperature and the magnetic field, and is expected to decrease as a function of I. The B_e component, however, only arises when the current is changed, and is expected to vary linearly as a function of (dI/dt). In addition, magnetization of the iron yoke and of the cryostat vessel enhances each of the field components. The iron and cryostat contributions are expected to follow the same dependence as the coil contributions, except at high transport currents, where saturation effect result in sizable distortions.

In this paper, we review the current dependence of the harmonic field coefficients measured on 5-cm-aperture, 15-m-long SSC dipole magnet prototypes. Over the last year and half, eighteen full-length prototypes have been produced and cold-tested at Brookhaven National Laboratory (BNL) and Fermi National Accelerator Laboratory (FNAL). The BNL and FNAL magnets rely on the same magnetic design,[1] but differ in some of their mechanical features.[2] For the BNL magnets, the yoke is split horizontally, and the collared-coil assembly is designed to interfere positively with the yoke along the vertical diameter. For the FNAL magnets, the yoke is split vertically, and the collar-yoke interference is along the horizontal diameter. After recalling a few definitions and describing the measurement procedure, we successively discuss the effects of persistent magnetization currents, eddy currents, and iron and cryostat magnetization. When appropriate, we also compare the behavior of the SSC dipole magnets to that of the superconducting dipole magnets for HERA.

DEFINITIONS AND MEASUREMENT PROCEDURE

In the long, almost straight, section of the magnet, the field can be considered as two-dimensional, and is conveniently represented by a multipole expansion

$$B_y + iB_x = 10^{-4} B_0 \sum_{n=0}^{+\infty} (b_n + ia_n) \left(\frac{x+iy}{r_0}\right)^n \quad , \qquad (1)$$

where B_x and B_y are the x- and y-components of the field, B_0 is the dipole field strength, b_n and a_n are the normal and skew 2(n+1)-pole coefficients, and r_0 is the reference radius. (For the SSC magnets, r_0 = 1 cm.) The symmetry of a dipole magnet is such that only even normal multipole coefficients, also called *allowed* multipole coefficients, are non-zero. In real magnets, manufacturing errors result in violations of the dipole symmetry which lead to non-zero *un-allowed* multipole coefficients.

An extensive set of magnetic measurements is performed on each of the SSC dipole magnet prototypes that are produced. For the full-length prototypes, the field harmonics are measured using the *mole* system developed by BNL.[3] This system consists of a tangential coil and two dipole bucking coils, which are 0.6 m in length, and rotate with a 3.2 s period. The measured data are corrected for centering errors of the mole using the feed-down from the 18- or 22-pole.

The measurements are taken following a test sequence which is representative of a SSC main ring operating cycle. The sequence starts with a *cleansing quench* to erase all previous magnetization currents. The magnet is then pre-cycled to a current of 6500 A, for a duration of 5 min, simulating a

*This work is supported by the U.S. Department of Energy under Contract No. DE-AC35-89ER40486.

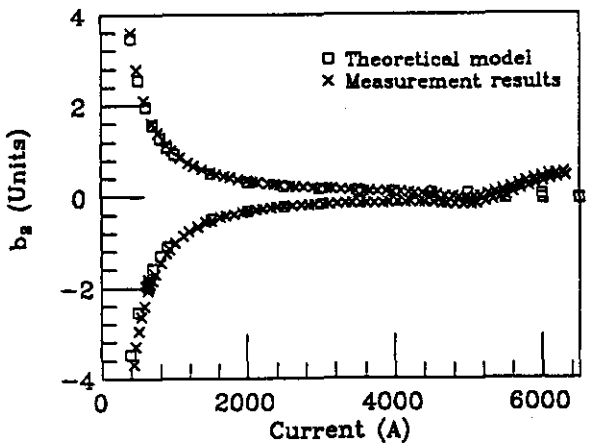

Fig. 1. Comparison between calculation and measurements of b_2 vs. current for FNAL magnet DCA317 at 4.35 K.

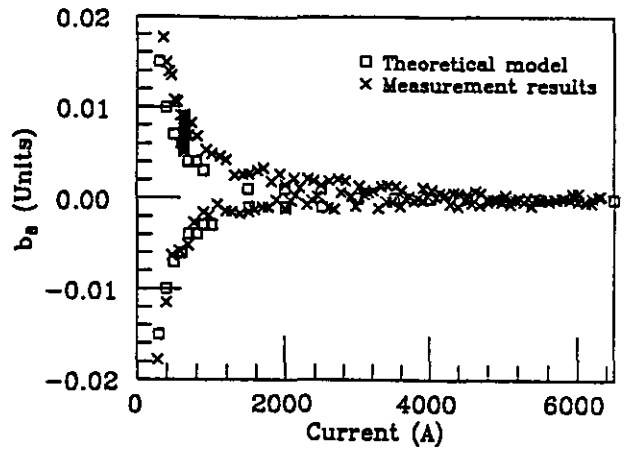

Fig. 2. Comparison between calculation and measurements of b_8 vs. current for FNAL magnet DCA317 at 4.35 K.

colliding beam cycle. It is then ramped down to 115 A for a 2-min dwell, ramped up to to 620 A and for a 10-min *pre-injection porch*, and ramped up again to 635 A for a 1-hour *injection porch*. At the end of the injection porch, the current is ramped up again to 6500 A, and then ramped down to 115 A, to simulate the next colliding beam cycle. The current ramp rate is 4 A/s, except for the ramp from 620 to 635 A, which is performed at 1 A/s. The data presented here paper include all the measurements taken starting from the 115-A dwell following the pre-cycle until the end of the test sequence.

EFFECTS OF PERSISTENT MAGNETIZATION CURRENTS

Persistent magnetization currents are generated at the periphery of the superconducting filaments in order to shield the filaments cores from the changes in local field resulting from current ramping. The magnetization currents form at the critical current density of the superconductor, and distribute themselves in order to produce, within the filaments, a dipole field opposite to the change in local B_t. Each filament, with its shells of persistent magnetization currents, then behaves as a magnetic doublet which slightly distorts the central field. Note, however, that the orientation of these magnetic doublets is determined by the transport-current flux lines, and thus, only the allowed multipole coefficients are expected to be affected.

Numerous models have been developed in order to predict the effects of persistent magnetization currents on the magnetic field. One of the most successful is that developed at Deutsches Elektronen-Synchrotron Laboratory (DESY), which reliably predicted the behavior of the superconducting magnets for HERA.[4] The same model is applied here toward understanding the persistent magnetization current effects in the SSC dipole magnets.

Figure 1 displays a comparison between calculation (squares) and measurements (crosses) of the normal sextupole coefficient (b_2) versus current for FNAL magnet DCA317 at 4.35 K. The calculation relies on the DESY model and uses actual values of critical current densities measured on short samples of the cables wound in magnet DCA317. To allow a direct comparison, the geometric component was subtracted,

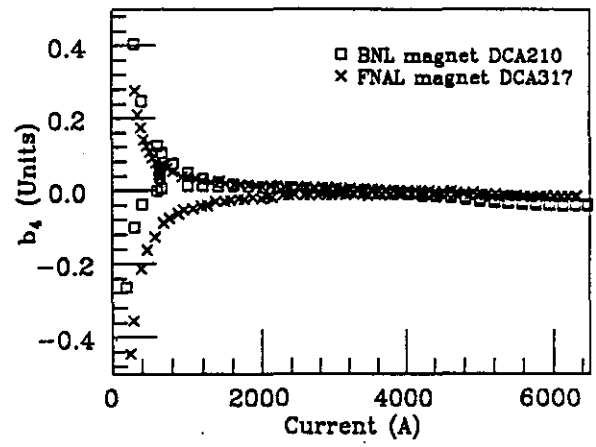

Fig. 3. Comparison of b_4 vs. current measurements for BNL magnet DCA210 and FNAL magnet DCA317 at 4.35 K.

i.e., the traces were shifted along the y-axis so that the average value between the two branches of the hysteresis is roughly zero. (For the two traces of Fig. 1, the lower branch corresponds to the current up-ramp; for currents above 4 kA, the experimental data show a clear rise, which, as discussed below, is attributed to iron yoke saturation effects.) Calculation and measurements are in good agreement. With the exception of the normal decapole coefficient (b_4) for the BNL magnets, a similar agreement is observed for all even normal multipoles where the model predicts persistent magnetization currents effects. The agreement remains good even for high order multipoles where the amplitude of the effect is quite small. Figure 2 shows, for instance, a comparison between calculation and measurements of the normal 18-pole coefficient (b_8) versus current for the same magnet and the same run as in Fig. 1. (For the two traces of Fig. 2, the upper branch correspond to the current up-ramp.) The data in Fig. 2 suggest that the random error of the measuring system can be estimated to be of the order of 0.002 units.

As we already mentioned, the only significant discrepancy that we observed between prediction and measurements is for the normal decapole coefficient (b_4) of the BNL magnets. As an illustration, Fig. 3 shows a comparison between

measurements on BNL magnet DCA210 (squares) and measurements on FNAL magnet DCA317 (crosses). (For the two traces of Fig. 3, the upper branch corresponds to the current up-ramp.) The b_4 hysteresis of the FNAL magnets appears symmetrical and in reasonable agreement with the prediction. The b_4 hysteresis of the BNL magnet, however, exhibits a sizable asymmetry between the up-and down-branches. Such asymmetry is observed on all the BNL magnets, and its origin is not yet understood.

EFFECTS OF CABLE EDDY CURRENTS

In the previous section, we discussed the effects of persistent magnetization currents, and we showed that, in most cases, there was a good agreement between theoretical predictions and measurement results. However, four dipole magnet prototypes (DCA312, DCA313, DCA314, and DCA315) exhibited field variations during current ramp at 4 A/s which significantly differed from the other prototypes, and which cannot be explained by the persistent magnetization current model.[5] It was also observed that this anomalous behavior only appeared while ramping the current, and that it ceased when the ramp was stopped.

In addition to this anomalous field behavior, these four magnets exhibited a dramatic degradation of their quench current as a function of ramp rate,[6] as well as large AC-losses.[7] A common feature of these four magnets is that they use inner cables made with strands coming from the same production batch of the same strand manufacturer. The strong ramp rate sensitivity and the large AC losses are attributed to unexpectedly large cable eddy currents,[6] and it is likely that these eddy currents are also responsible for the anomalous field behavior.[5]

The inner (outer) cables used in SSC magnets consist of 30 (36) bare strands, twisted together, and shaped into a flat, two-layer, slightly keystoned cable. The cable mid-thickness is smaller than twice the strand diameter, and the contact surfaces at the crossovers between the strands of the two layers are relatively large. Also, during magnet assembly the coils are pre-compressed azimuthally.[2] Large pressures are thus applied perpendicularly to the cables, which keep the strands firmly in contact. The large contact surfaces and high pressures eventually result in low contact resistances at the strand crossovers, which couple the cable strands. Loops are thus formed where significant eddy currents can take place when subjected to a varying field. Assuming that the eddy currents flowing from one strand to the other always pass through the crossover resistance, the cable can be represented as a simple network of resistances. The cable eddy currents, and their effects on the magnetic field, can then be computed by combining this model circuit with a two-dimensional field calculation.[5]

Eddy-current fields arise when the transport current, I, is changed, and they are expected to vary linearly as a function (dI/dt). In the first approximation, a current ramp at a constant rate should result in a constant eddy current field. Furthermore, if we assume that the crossover resistance, r_c, is uniform throughout the coil, the eddy current distribution follows the dipole symmetry and only effects the allowed multipole coefficients. For a 5-cm-aperture SSC dipole magnet, the eddy-current sextupole and decapole fields at a 1-cm radius, $B_{2e} = B_0\, b_{2e}$ and $B_{4e} = B_0\, b_{4e}$, can be estimated to be[8]

$$B_{2e}(r_0 = 1\text{ cm}) = 0.4\,(dI/dt)/r_c \quad , \tag{2a}$$

$$B_{4e}(r_0 = 1\text{ cm}) = -0.02\,(dI/dt)/r_c \quad , \tag{2b}$$

where B_{2e} and B_{4e} are in Gauss, $\partial I/\partial t$ is in A/s, and r_c is in $\mu\Omega$. The corresponding power per unit length, W, dissipated by the eddy currents in the crossover resistances is

$$W = 2.5\text{x}10^{-3}\,(dI/dt)^2/r_c \quad , \tag{2c}$$

where W is in W/m

As a comparison, estimates of the same quantities for a HERA dipole magnet are (in the same units as above)[8]

$$B_{2e}(r_0 = 2.5\text{ cm}) = 0.4\,(dI/dt)/r_c \quad , \tag{3a}$$

$$B_{4e}(r_0 = 2.5\text{ cm}) = -0.05\,(dI/dt)/r_c \quad , \tag{3b}$$

$$W = 1.0\text{x}10^{-3}\,(dI/dt)^2/r_c \quad . \tag{3c}$$

The cables used in the HERA magnets have their strands coated with a thin layer of 95 wt% silver–5 wt% tin solder called *stabrite*. The purpose of this coating is to prevent the uncontrolled formation of a copper oxide layer at the strand periphery, and to make the crossover resistance as uniform as possible along the cable and throughout the cured coil. The drawback, however, is that it yields a low value of r_c. Measurements on a short sample of HERA cable show $r_c = 2.1 \pm 0.5\ \mu\Omega$.[9] Introducing this number in Eq. (3a) lets us predict $\Delta B_{2e}(r_0 = 2.5\text{ cm}) = 0.2$ Gauss/(A/s). Measurements that were recently performed on a HERA dipole magnet showed indeed $\Delta B_{2e}(r_0 = 2.5\text{ cm}) = 0.2$ Gauss/(A/s).[10] This good agreement between calculation and measurements gives us some confidence that the model that was developed[5] can adequately predict the effects of cable eddy currents.

Unlike the HERA cables, the strands of the SSC cables are bare. They are thus free to develop a layer of copper oxide during the various steps of cable manufacturing and magnet assembly. Little is known, however, on the parameters that determine the thickness of this layer. Speculations are that it strongly depends on the purity of the copper matrix and whether the strands are annealed after the final drawing. It is also believed that the copper oxide layer depends strongly on the parameters of the coil curing cycle. In principle, the presence of this copper oxide layer can yield crossover resistances that are several orders of magnitude larger than that obtained with stabrite-coated strands. The drawback, however, is that it is difficult to control, and can lead to non-uniformities, either along the cable length, or from turn to turn in the cured coil. A distribution of crossover resistance that varies from turn to turn, as a function of the azimuth, results in an eddy-current distribution that violates the dipole symmetry, thereby effecting all multipole coefficients.

Figure 4 shows a summary plot of skew quadrupole coefficient (a_1) versus current for two anomalous SSC dipole magnet prototypes (magnets DCA314 and DCA315) compared to a normally-behaved one (magnet DCA317). Although we are not expecting any sizable effects from the persistent magnetization currents, magnets DCA314 and DCA315 both

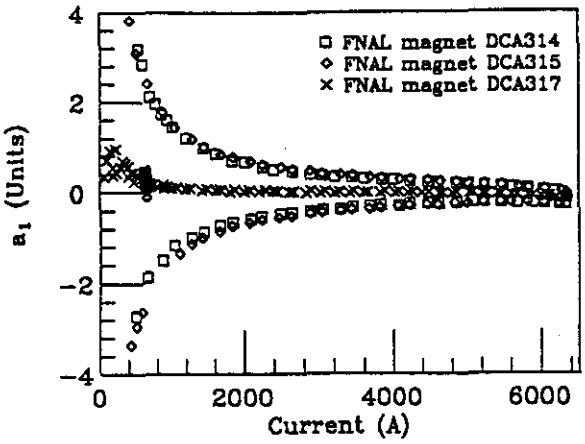

Fig. 4: Summary of a_1 vs. current for two anomalous magnets (magnets DCA315 and DCA314) and a normally-behaved one (magnet DCA317).

exhibit a very large hysteresis. Furthermore, these two hystereses appear to be described in opposite direction: for magnet DCA314, the current up-ramp corresponds to the upper branch, while, for magnet DCA315, it corresponds to the lower branch. As described in reference 5, this anomalous a_1 behavior can be explained in terms of top/bottom asymmetric eddy currents resulting from a non-uniform distribution of crossover resistances. (For currents above 4 to 5 kA, the three traces of Fig. 4 show a tendency to dip, which, as described below, is attributed to flux leakage asymmetry between magnet cold mass and cryostat.)

For each of the anomalous magnets, it is in fact possible to determine an azimuthal distribution of crossover resistance, that results in a distribution of eddy currents, which can explain the observed behavior of all the multipole coefficients and is consistent with the measured AC-losses.[5] Also, for each of the anomalous magnets, the model accurately predicts in which half coil the high ramp rate quenches should originate. This consistent agreement between simulations and experimental data gives us good confidence that we have identified the cause of the poor AC performance of these four magnets. Efforts are now underway to determine how to avoid these non-uniformities in the crossover resistance.

EFFECTS OF IRON YOKE AND CRYOSTAT

Above 4 kA, the transport-current field produced by the coil is large enough to saturate the iron yoke. Due to a high field at the pole, iron saturation is first felt there, which results in a positive contribution to the normal sextupole coefficient (b_2). The return flux through the midplane causes it to saturate as well. At currents of the order of 6500 A, midplane saturation overcomes pole saturation resulting in a net negative b_2. The present magnetic design, however, includes cut-outs at the midplane of the iron yoke that are designed to force the midplane saturation to occur at a lower current, and thus to compensate partially the effect on b_2 of the pole plane saturation.[1] This compensation was very successfully implemented on the BNL-design magnets, for which the b_2 change due to iron saturation does not exceed 0.1 units. As can be seen in Fig. 1, the FNAL-design magnets do exhibit a larger change (of the order of 0.5 units at 6500 A), but the observed b_2 saturation conforms to prediction. The iron saturation also effects the normal decapole coefficient (b_4), but to a lesser extent. For both designs, the observed b_4 saturation conforms to prediction.

Another predicted effect is that, at high current, flux lines start to leak out of the cold mass. As the cold mass is not centered within the cryostat, and the cryostat itself is made of low carbon steel, the flux lines become slightly distorted. This distortion, which violates the top/bottom symmetry, results in a decrease of a_1[11] which, for the 5-cm-aperture dipole magnets, is estimated between 0.1 and 0.2 units. For the normally-behaved magnet of Fig. 4 (DCA317), the observed a_1 saturation is within prediction.

CONCLUSION

For most of the 5-cm-aperture, 15-m-long SSC dipole magnet prototypes tested so far, the observed current dependence of the harmonic field coefficients can be described by persistent magnetization currents and of iron yoke and cryostat vessel magnetization. A few prototypes, however, exhibit anomalous behavior of their field harmonics during current ramp at 4 A/s. These anomalies, which cease when the current ramp is stopped, can be explained in terms of cable eddy currents. Efforts are now under way to determine the cable parameters that need to be mastered in order to control them.

REFERENCES

[1] R.C. Gupta, S.A. Kahn, and G.H. Morgan, "SSC 50 mm Dipole Cross Section," *Supercollider 3*, J. Nonte, ed., 1991, pp. 587-599.

[2] A. Devred, T. Bush, *et al.*, "Review of SSC Dipole Magnet Mechanics and Quench Performance," to appear in *Supercollider 4*, J. Nonte, ed., 1992.

[3] G. Ganetis, J, Herrera, *et al.*, "Field Measuring Probe for SSC Magnets," Proc. 1987 IEEE Part. Acc. Conf., 1987, pp. 1393-1395.

[4] H. Brück, D. Gall, *et al.*, "Persistent Magnetization Effects in the Superconducting HERA Magnets and Correction Coils," Proc. 2nd Eur. Part. Acc. Conf., 1990, pp. 1160-1162.

[5] T. Ogitsu, Y. Zhao, *et al.*, presented at the ICFA workshop on AC Superconductivity, KEK, National Laboratory for High Energy Physics, Tsukuba, Japan, June 23-25, 1992.

[6] W. Nah, A. Akhmetov, *et al.*, "Quench Characteristics of 5-cm-Aperture, 15-m-Long SSC Dipole Magnet Prorotypes," in these Proceedings.

[7] J. Ozelis, S.W. Delchamps, *et al.*, "AC Loss Measurements of Model and Full Size 50 mm SSC Collider Dipole Magnets at Fermilab," in these Proceedings.

[8] T. Ogitsu, private communication.

[9] A. Ghosh, private communication.

[10] H. Brück, private communication.

[11] R.C. Gupta, J.G. Cottingham, *et al.*, " A Comparison of Calculations and Measurements of the Field Harmonics as a Function of Current in the SSC Dipole Magnets," Proc. 1991 IEEE Part. Acc. Conf., 1991, pp. 42-44.

ENHANCED QUENCH PROPAGATION VELOCITY

R.G. Mints[†‡], A.A. Akhmetov[†] and A. Devred[†]
[†]SSC Laboratory*, Dallas, TX, USA
[‡]School of Physics and Astronomy, Tel-Aviv University, Tel-Aviv, Israel

Abstract—Quench propagation velocity in conductors having a large amount of stabilizer outside the multifilamentary area is considered. It is shown that the current redistribution process between the multifilamentary area and the stabilizer can strongly effect the quench propagation. A criterion is derived determining the conditions under which the current redistribution process becomes significant, and a model of effective stabilizer area is suggested to describe its influence on the quench propagation velocity. As an illustration, the model is applied to calculate the adiabatic quench propagation velocity for a conductor having a multiply connected stabilizer, consisting of an inner core and an outer sheath.

I. INTRODUCTION

The development of conductors with aluminium superstabilizer for applications, such as detector magnets for high energy physics [1], energy storage devices [2-4], and others, has led to new problems. One of them is the effect of current redistribution process between the superconductor and stabilizer on the quench propagation [5, 6].

The quench propagation velocity is determined by the Joule heating in the vicinity of the transition front. During the transition from the superconducting to the resistive state, the current is redistributed from the superconductor to the stabilizer. This redistribution occurs in two phases. First, the current is expelled from the superconducting filaments to the copper in the multifilamentary area. Second, the current diffuses into the stabilizer outside the multifilamentary area. If the interfilament spacing is small, the first phase is very fast. On the other hand, if most of the stabilizer is located outside of the multifilamentary area, the second phase can be relatively long. In the vicinity of the transition front, where the quench-driving heat release occurs, the current may thus remain confined in a small fraction of stabilizer around the multifilamentary area. This results in a relatively high local value of Joule heating, leading to high quench propagation velocity [6].

In this paper, we shall consider the case where the quench propagation is effected by the current redistribution process. We shall introduce the characteristic velocity at which this process becomes significant. We shall introduce a model of effective stabilizer area for fast quench propagation. We apply this model to calculate the adiabatic quench velocity for a conductor having a multiply connected stabilizer, consisting of an inner core and an outer sheath, as depicted in Fig. 1 [7].

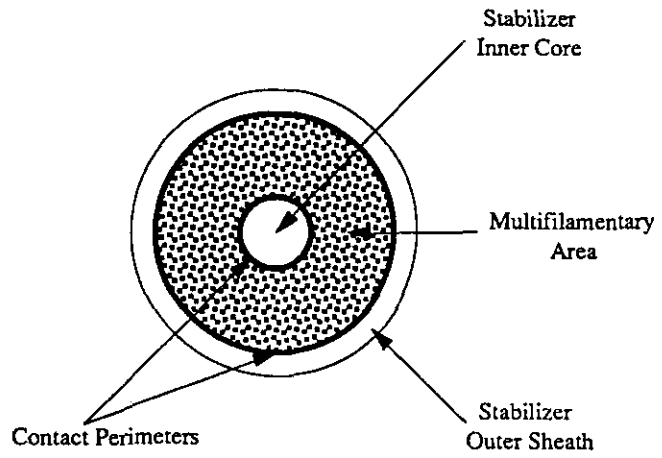

Figure 1: The conductor cross-section.

II. HIGHLY STABILIZED CONDUCTORS

Most of the papers on quench propagation velocity consider the current redistribution process as instantaneous (see the review in reference [8]). To discuss the applicability of this assumption, let us estimate the characteristic times of the phenomena involved. The current redistribution time, t_d, may be estimated as

$$t_d = \frac{\mu_0 d^2}{\rho_n}, \tag{1}$$

where ρ_n is the resistivity, and d is the effective thickness of the stabilizer. In case of the conductor shown in Fig. 1 there are two effective thicknesses: d_i for the inner core and d_o for the outer sheath, given by

$$d_i = \frac{A_n^i}{P_n^i}, \qquad and \qquad d_o = \frac{A_n^o}{P_n^o}, \tag{2}$$

where A_n^i and A_n^o, and P_n^i and P_n^o are the cross-sectional areas, and contact perimeters of the stabilizer (see Fig. 1).

*Operated by Universities Research Association, Inc., for the U.S. Department of Energy, under contract No. DE-AC35-89ER40486
Manuscript received August 24, 1992

The characteristic time associated with the quench propagation, t_p, is given by

$$t_p = \frac{L}{v}, \tag{3}$$

where v is the quench propagation velocity, and L is the thickness of the zone where the quench–driving heat release occurs. In other words, L is the thickness of the region, in the vicinity of the transition front from the resistive to the superconducting state, where the Joule heating determining the propagation velocity takes place.

In case of instantaneous current redistribution, the power Q of the Joule heating in the conductor is given by

$$Q = \rho \frac{I}{A} \begin{cases} 0, & T < T_{ci}; \\ I_c \dfrac{T - T_{ci}}{T_c - T_0}, & T_{ci} < T < T_c; \\ I, & T_c < T, \end{cases} \tag{4}$$

where

$$T_{ci} = T_c - i\,(T_c - T_0), \qquad i = \frac{I}{I_c}. \tag{5},$$

Here T_0 is the coolant temperature, T_c is the critical temperature at the given field and T_0, I is the transport current, I_c is the critical current at the given field and T_0, ρ is the longitudinal electrical resistivity of the conductor, and A is the conductor cross-sectional area. An expression of ρ is given by

$$\rho = \frac{A \rho_n \rho_s}{A_n \rho_s + A_s \rho_n}, \tag{6}$$

where A_n is the total cross-sectional area of stabilizer, and A_s and ρ_s are the cross-sectional area and the resistivity of the multifilamentary area. In this paper, we shall represent the power of the Joule heating in the conductor as a step function of temperature

$$Q = \rho \frac{I^2}{A} \begin{cases} 0, & T < T_t; \\ 1, & T_t < T. \end{cases} \tag{7}$$

The transition temperature, T_t, is determined so that the propagation velocity derived using Eq. (7) is equal to that derived using Eq. (4). It can be shown [9] that

$$T_t = T_{ci} + \alpha(i)\,(T_c - T_{ci}), \tag{8}$$

where α is a dimensionless parameter that only depends on i. This dependence is presented in Fig. 2.

In most cases of practical interest, the cooling conditions are weak. Then, L is determined by the thermal diffusion along the conductor, and can be estimated as [6]

$$L = \frac{\kappa}{Cv}, \tag{9}$$

where κ and C are the thermal conductivity and the heat capacity per unit volume averaged over the conductor cross-section, and taken at the given field and T_t.

Thus, the current redistribution process can be considered as instantaneous, only if the dimensionless parameter

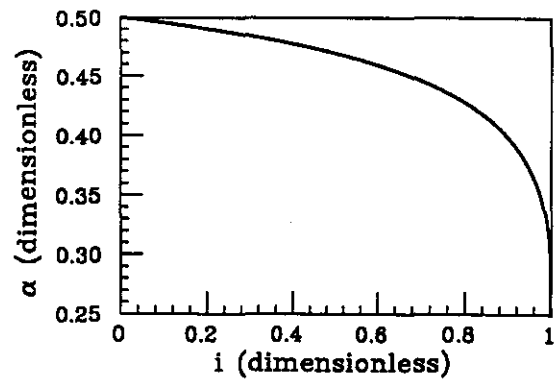

Figure 2: The dependence of the parameter α on the dimensionless current i.

$\tau = t_d/t_p$ is less than one. Using Eqs. (1) to (3), and Eq. (9), it is convenient to rewrite τ as

$$\tau = \frac{\mu_0 C d^2}{\kappa \rho_n} v^2 = \left(\frac{v}{v_c}\right)^2, \tag{10}$$

where we have introduced the characteristic velocity v_c

$$v_c = \frac{1}{d}\sqrt{\frac{\kappa \rho_n}{\mu_0 C}}. \tag{11}$$

For the conductor considered above there are two characteristic velocities: one for the inner core, v_c^i, and one for the outher sheath, v_c^o. Using Eq. (8) and the data from [7] (assuming an interfilament spacing of $2\,\mu m$, a critical current density $j_c(5\,T, 4.2\,K) = 2.75 \cdot 10^9\,A/m^2$ and a constant external magnetic field of $5\,T$) one gets: $v_c^i \approx 50 m/s$ and $v_c^o \approx 25 m/s$.

Let us now consider the case of instantaneous current redistribution. The quench propagation velocity is determined by the Joule heating in the vicinity of the transition front. The thickness of this region is L, and, the power of the quench-driving heat release, q, can be written as

$$q = \rho \frac{I^2}{A} L. \tag{12}$$

On the other hand, q is equal to the heat flux which heats up the superconducting zone to the transition temperature. It follows

$$q = vA\Delta H, \tag{13}$$

where

$$\Delta H = \int_{T_0}^{T_t} C\,dT, \tag{14}$$

is the difference in enthalpy per unit volume of conductor between T_0 and T_t. For adiabatic cooling conditions, the value of L is given by Eq. (9). Equating the two expressions of q, and substituting the expression of L, lead to

$$v = \frac{I}{A}\sqrt{\frac{\kappa \rho}{C \Delta H}}. \tag{15}$$

In this model, the maximum of the quench propagation velocity, v_m, is obtained for $I = I_c$. Let us estimate v_m for the conductor considered above. Using the data from [7] and Eq. (15), one gets: $v_m \approx 50 m/s$.

For adiabatic cooling conditions, a criterion defining highly stabilized conductors may be derived by comparing v_m and v_c. Let us define dimensionless parameter β

$$\beta = \left(\frac{v_m}{v_c}\right)^2. \tag{16}$$

Then, a highly stabilized conductor is a conductor with β larger than one. Combining Eqs. (11) and (15) leads to the following criterion

$$\beta = \frac{\rho}{\rho_n}\left(\frac{d}{A}\right)^2 \frac{\mu_0 I_c^2}{\Delta H_c} \geq 1, \tag{17}$$

where ΔH_c is calculated by means of Eq. (14) at $I = I_c$. For the conductor considered above: $\beta_i \approx .91$ for the inner core, and $\beta_o \approx 3.7$ for the outer sheath. It thus appears that actual conductors can exibit quench propagation velocities larger than v_c.

III. EFFECTIVE STABILIZER AREA MODEL

Let us now consider the case where the current redistribution has to be taken into account while calculating the quench propagation velocity, *i.e.*, $v \gg v_c$. Then, in the vicinity of the transition front, the current remains confine to a certain fraction of stabilizer around the multifilamentary area, leading to non-uniform quench-driving heat release. The cross-sectional area occupied by the current is determined by the parameter, τ. The larger τ, *i.e.*, the larger the ratio of v to v_c, the smaller the fraction of stabilizer where the current has diffused.

In most cases of practical interest, the cooling is weak and, at the same time, the ratio of the transverse thermal diffusivity to the magnetic flux diffusivity is high. It results that the temperature distribution over the conductor cross-sectional area is uniform, even if the heat release is non-uniform.

The main difference between highly stabilized and conventional conductors is thus the non-uniformity of the quench-driving heat release. To find the exact expression of the Joule heating, we should solve the system of Maxwell's and heat diffusion equations. For most cases of practical interest, it cannot be done analytically, and is a complicated problem for numerical analysis.

In this paper, we shall calculate the Joule heating considering that the current is uniformly redistributed between the multifilamentary area and a certain area of the stabilizer, which we shall introduce as an effective area, A_{eff}. As the fraction of the stabilizer where the current has diffused depends on the quench propagation velocity, the effective area of the stabilizer is determined by the ratio v/v_c. In case of the conductor shown in Fig. 1 we have

$$A_{\text{eff}} = A^i_{\text{eff}} + A^o_{\text{eff}}, \tag{18}$$

$$A^i_{\text{eff}} = A^i_n\, f_i\left(\frac{v}{v^i_c}\right), \qquad A^o_{\text{eff}} = A^o_n\, f_o\left(\frac{v}{v^o_c}\right), \tag{19}$$

where A^i_{eff} and A^o_{eff} are the effective stabilizer areas, and v^i_c and v^o_c are the critical velocities for the inner core and outer sheath.

To find an expressions for f_i and f_o, let us first discuss the asymptotic behavior of f_i and f_o. When the ratios v/v^i_c and v/v^o_c are small, the current redistribution process is almost instantaneous, and the current occupies the whole stabilizer cross-sectional area, *i.e.*, A^i_{eff} tends towards A^i_n, and A^o_{eff} tends towards A^o_n. We thus have

$$f_i\left(\frac{v}{v^i_c}\right) = 1, \qquad \text{for} \quad \frac{v}{v^i_c} \to 0, \tag{20 a}$$

$$f_o\left(\frac{v}{v^o_c}\right) = 1, \qquad \text{for} \quad \frac{v}{v^o_c} \to 0. \tag{20 b}$$

On the other hand, when the ratios v/v^i_c and v/v^o_c are large, the current only diffuses into thin layers of stabilizer, l_i and l_o, and the current redistribution process can be treated as in the case of a semi–infinite slab of stabilizer. Then, l_i and l_o are determined by the magnetic flux diffusion length for a characteristic time of the order of t_p

$$l_i = \sqrt{D_m t_p} = \frac{A^i_n}{P^i_n}\frac{v^i_c}{v}, \tag{21 a}$$

$$l_o = \sqrt{D_m t_p} = \frac{A^o_n}{P^o_n}\frac{v^o_c}{v}. \tag{21 b}$$

Thus, the effective areas, *i.e.*, the cross–sectional areas of stabilizer occupied by the current are

$$A^i_{\text{eff}} = l_i P^i_n = A^i_n \frac{v^i_c}{v}, \tag{22 a}$$

$$A^o_{\text{eff}} = l_o P^o_n = A^o_n \frac{v^o_c}{v}, \tag{22 b}$$

and, it comes

$$f_i\left(\frac{v}{v^i_c}\right) = \frac{v^i_c}{v}, \qquad \text{for} \quad \frac{v}{v^i_c} \to \infty. \tag{23 a}$$

$$f_o\left(\frac{v}{v^o_c}\right) = \frac{v^o_c}{v}, \qquad \text{for} \quad \frac{v}{v^o_c} \to \infty. \tag{23 b}$$

Having determined the asymptotic dependencies for small and large values of v/v^i_c and v/v^o_c, we shall now define f_i and f_o for the full range of velocities. To match smoothly Eqs. (20 a) and (23 a), and Eqs. (20 b) and (23 b) we suggest the following functions

$$f_i\left(\frac{v}{v^i_c}\right) = \frac{I_1\left(2\frac{v^i_c}{v}\right)}{I_0\left(2\frac{v^i_c}{v}\right)}, \tag{24 a}$$

$$f_o\left(\frac{v}{v_c^o}\right) = \tanh\left(\frac{v_c^o}{v}\right), \qquad (24\,b)$$

where $I_0(x)$ and $I_1(x)$ are modified Bessel functions of order 0, 1. Note, that the Eq. (24 a) is a generalization of Eq. (24 b) for the case of cylindrical geometry.

IV. ADIABATIC QUENCH PROPAGATION

In this section, we shall apply the above model of effective stabilizer area to the computation of the adiabatic quench propagation velocity. To do it, we have to calculate the quench-driving heat release. In the case of adiabatic cooling conditions, it is given by Eq. (12). Then, substituting A_n by A_{eff} in Eq. (12), it comes

$$q = \frac{\rho_n \rho_s I^2}{A_{\text{eff}}\rho_s + A_s \rho_n} \frac{\kappa}{Cv}, \qquad (25)$$

where we have replaced L by Eq. (9). An equation determining v can be derived by equating Eqs. (25) and (13), and replacing A_{eff} by Eq. (18). It comes

$$v = \frac{I}{A}\sqrt{\frac{\kappa\rho}{C\Delta H}} \sqrt{\frac{1+r}{1+r\left[x_n^i\, f_i\left(\frac{v}{v_c^i}\right) + x_n^o\, f_o\left(\frac{v}{v_c^o}\right)\right]}}, \qquad (26)$$

where

$$r = \frac{A_n \rho_s}{A_s \rho_n} \gg 1, \qquad x_n^i = \frac{A_n^i}{A_n}, \qquad x_n^o = \frac{A_n^o}{A_n}. \qquad (27)$$

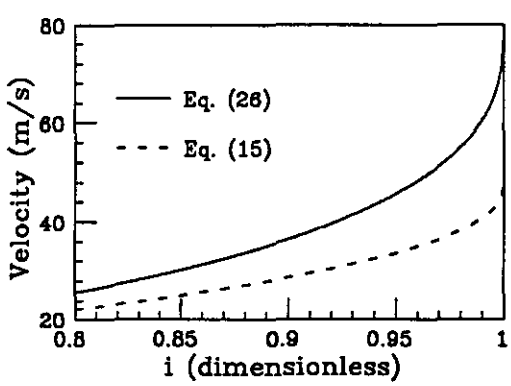

Figure 3: The dependence of the quench propagation velocity v on the dimensionless current i.

To illustrate these results, Fig. 3 shows plots of the quench propagation velocity as a function of the dimensionless current i for the conductor considered above. The solid line represents the velocity calculated by the combination of Eqs. (24 a, b) and (26), which takes into account the current redistribution process. The dashed line represents the velocity calculated by means of Eq. (15), which assumes an instantaneous current redistribution. As can be seen in Fig. 3, the difference in the results can be up to 1.6 times. Note that Eq. (26) shows that the velocity depends on the distribution of stabilizer between the inner core and the outher sheath, *i.e.*, v is a function of x_n^i or $x_n^o = 1 - x_n^i$. This dependence is illustrated in Fig. 4 (for $I = I_c$). It can be seen that v goes through a minimum.

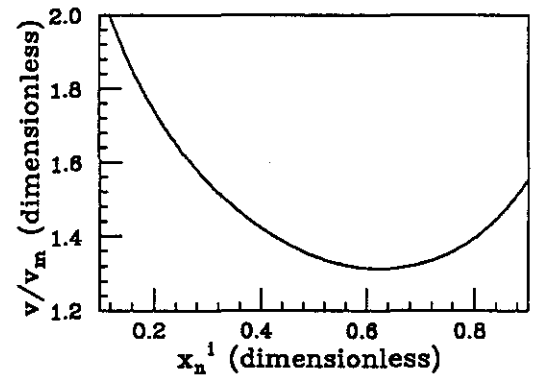

Figure 4: The dependence of the ratio $v(I_c)/v_m(I_c)$ on x_n^i.

References

[1] A. Devred, Proceedings of the 11th International Conference on Magnet Technology (MT–11), Tsukuba, Japan, August 28–September 1, 1989, edited by T. Sekiguchi and S. Shimamoto, Elsevier Applied Science, New–York, 78 (1990).

[2] C.A. Luongo, R.J. Loyd, and C.L. Chang, IEEE Trans. Magn. **MAG-25** 1576, 1989.

[3] X. Huang, Y.M. Eyssa, IEEE Trans. Magn. **MAG–27** 2304, 1991.

[4] Raz Kupferman, R.G. Mints, and E.J. Ben-Jacob, J. Appl. Phys. **70** 7484, 1991.

[5] L. Dresner, Cryogenics **31** 489, 1991.

[6] R.G. Mints, T. Ogitsu, and A. Devred, Cryogenics **32** (to be published).

[7] D. ter Avest, G. Schoenmaker, H.G. Knoopers, and L.J.M. van de Klundert, Advances in Cryogenic Engineering **38 B**, 737, 1992.

[8] A.Vl. Gurevich and R.G. Mints, Rev. Mod. Phys. **59** 941, 1987.

[9] A. Devred, IEEE Trans. Magn. **MAG–25** 1698, 1989.